Depolarization-induced Calcium Responses in Sympathetic Neurons: Relative Contributions from Ca^{2+} Entry, Extrusion, ER/Mitochondrial Ca^{2+} Uptake and Release, and Ca^{2+} Buffering

Michael Patterson,[1] James Sneyd,[2] and David D. Friel[1]

[1]Department of Neurosciences, Case Western Reserve University, Cleveland, OH 44106
[2]Department of Mathematics, University of Auckland, Auckland, New Zealand

Many models have been developed to account for stimulus-evoked $[Ca^{2+}]$ responses, but few address how responses elicited in specific cell types are defined by the Ca^{2+} transport and buffering systems that operate in the same cells. In this study, we extend previous modeling studies by linking the time course of stimulus-evoked $[Ca^{2+}]$ responses to the underlying Ca^{2+} transport and buffering systems. Depolarization-evoked $[Ca^{2+}]_i$ responses were studied in sympathetic neurons under voltage clamp, asking how response kinetics are defined by the Ca^{2+} handling systems expressed in these cells. We investigated five cases of increasing complexity, comparing observed and calculated responses deduced from measured Ca^{2+} handling properties. In Case 1, $[Ca^{2+}]_i$ responses were elicited by small Ca^{2+} currents while Ca^{2+} transport by internal stores was inhibited, leaving plasma membrane Ca^{2+} extrusion intact. In Case 2, responses to the same stimuli were measured while mitochondrial Ca^{2+} uptake was active. In Case 3, responses were elicited as in Case 2 but with larger Ca^{2+} currents that produce larger and faster $[Ca^{2+}]_i$ elevations. Case 4 included the mitochondrial Na/Ca exchanger. Finally, Case 5 included ER Ca^{2+} uptake and release pathways. We found that $[Ca^{2+}]_i$ responses elicited by weak stimuli (Cases 1 and 2) could be quantitatively reconstructed using a spatially uniform model incorporating the measured properties of Ca^{2+} entry, removal, and buffering. Responses to strong depolarization (Case 3) could not be described by this model, but were consistent with a diffusion model incorporating the same Ca^{2+} transport and buffering descriptions, as long as endogenous buffers have low mobility, leading to steep radial $[Ca^{2+}]_i$ gradients and spatially nonuniform Ca^{2+} loading by mitochondria. When extended to include mitochondrial Ca^{2+} release (Case 4) and ER Ca^{2+} transport (Case 5), the diffusion model could also account for previous measurements of stimulus-evoked changes in total mitochondrial and ER Ca concentration.

The Journal of General Physiology

INTRODUCTION

Ionized free calcium (Ca^{2+}) is a ubiquitous signaling ion that serves both as an important charge carrier and as a chemical intermediate that links a variety of physiological stimuli to their intracellular effectors (Berridge, 1998; Carafoli et al., 2001). One of the central problems in Ca^{2+} signaling research is to understand how Ca^{2+} handling mechanisms function together in intact cells to define the spatiotemporal properties of stimulus-evoked $[Ca^{2+}]$ responses. In its signaling capacity, Ca^{2+} acts by binding to specific sites whose occupancy translates the Ca^{2+} signal into downstream cellular effects. Since binding site occupancy depends on the history of the free Ca^{2+} concentration ($[Ca^{2+}]$), Ca^{2+} dynamics are critical. As a result, $[Ca^{2+}]$ is tightly regulated by various Ca^{2+} channels, pumps, exchangers (here collectively referred to as transporters), and buffers that determine the proportion of Ca^{2+} that is free vs. bound.

Mathematical modeling provides a useful tool for investigating the basis of Ca^{2+} dynamics, making it possible to address topics that would be difficult to investigate in other ways. For example, model calculations can be used to test if a particular combination of transport and buffering systems can support a qualitative mode of Ca^{2+} dynamics, such as Ca^{2+} oscillations (Goldbeter et al., 1990; Dupont and Goldbeter, 1993). Modeling can also clarify how individual transport systems contribute to evoked Ca^{2+} responses (Colegrove et al., 2000b). This can be difficult to do simply by observing the effects of specific inhibitors on evoked Ca^{2+} responses because of secondary changes in the activity of other Ca^{2+} handling systems that arise because of their dependence on $[Ca^{2+}]$. A third area well suited to modeling is the investigation of how quantitative changes in the functional properties of Ca^{2+} regulatory systems influence Ca^{2+} dynamics in genetic disease. Here it can be asked if a Ca^{2+} regulatory syndrome is consistent with the

Correspondence to David Friel: ddf2@case.edu

M. Patterson's present address is Department of Neurobiology, Duke University, Durham, NC.

Abbreviations used in this paper: CICR, Ca^{2+}-induced Ca^{2+} release; FCCP, carbonyl cyanide *p*-trifluoromethoxyphenylhydrazone; NCX, plasma membrane Na/Ca exchanger; PMCA, plasma membrane Ca^{2+} ATPase; SERCA, sarco/endoplasmic reticulum Ca^{2+} ATPase; Tg, thapsigargin.

operation of a single defective gene product, or requires consideration of compensatory mechanisms as well. Finally, realistic models of Ca^{2+} dynamics can be used to test in silico how selective pharmacological perturbations of Ca^{2+} transport and buffering are expected to impact Ca^{2+} signaling in intact cells.

There is a long and productive history of modeling in Ca^{2+} signaling research. For example, mathematical models have been used to examine qualitative properties of Ca^{2+} dynamics under the control of various Ca^{2+} handling systems whose properties are specified based on literature values from multiple cell types. This approach has helped build intuition about Ca^{2+} signal generation, and has clarified the conditions required for generation of Ca^{2+} oscillations and waves (Keener and Sneyd, 1998). There has been less progress, however, in understanding how the specific Ca^{2+} regulatory mechanisms that function together in intact cells define stimulus-evoked $[Ca^{2+}]$ elevations, although important contributions have been made in this area by studies in muscle cells (Kovacs et al., 1983; Sipido and Wier, 1991; Schuhmeier and Melzer, 2004). There are several reasons for this, all of which represent a lack of experimental data for constraining model development, rather than a lack of mathematical tools: (a) technical difficulties in measuring and characterizing the relevant Ca^{2+} fluxes in intact cells, particularly those representing Ca^{2+} uptake and release by intracellular stores; nevertheless, several groundbreaking studies clarified how this can be done (Herrington et al., 1996; Sipido and Wier, 1991; Kovacs et al., 1983); (b) lack of information about the important "independent" variables that control the activity of these regulatory systems in their normal intracellular milieu, and how activity depends on these variables; and (c) poor consensus regarding the functional role of Ca^{2+} regulatory events on small vs. large space and time scales. Given that comprehensive descriptions of Ca^{2+} regulation that apply over all distance and time scales are currently unavailable, descriptions that apply over intermediate ranges of distance and time would be of considerable practical value. For example, they would serve as important limiting cases for models that address signaling in microdomains of space and time, and facilitate rigorous testing of hypotheses derived from experimental studies. Indeed, one of the most revealing ways to evaluate the importance of a proposed Ca^{2+} handling mechanism for Ca^{2+} signal generation is to determine if it is necessary to reconstruct measured Ca^{2+} responses. Of course, this requires a "complete" description of the regulatory mechanisms operating in the cell under study, since exclusion of any critical pathway would render such a reconstruction impossible.

Our previous work has described approaches for measuring and characterizing Ca^{2+} fluxes and buffering strength in sympathetic neurons (Colegrove et al., 2000a, Albrecht et al., 2002). The purpose of the present study is to determine if these characterizations are sufficient, when taken together, to account quantitatively for depolarization-induced Ca^{2+} responses in these cells. We found that when these characterizations are incorporated into a model that assumes cytoplasmic Ca^{2+} is uniformly distributed, it was possible to account quantitatively for responses to weak depolarization, but not responses to stronger depolarization when radial $[Ca^{2+}]_i$ gradients are expected to be steep. However, we could account for these responses using a more general model that explicitly considers radial differences in Ca^{2+} concentration. The two models yielded very similar $[Ca^{2+}]_i$ trajectories for weak depolarization, indicating that the uniform model describes a limiting case of the diffusion model when $[Ca^{2+}]_i$ gradients are shallow. Overall, the results provide a core description of neuronal Ca^{2+} regulation that can be applied to other cells as more information becomes available regarding cell type–specific regulatory mechanisms and their cellular distribution.

MATERIALS AND METHODS

Cell Preparation

Bullfrog sympathetic neurons were dissociated enzymatically and placed in culture for up to 1 wk as described previously (Colegrove et al., 2000a). All procedures conform to guidelines established by our Institutional Animal Care and Use Committee.

Cytosolic Calcium Measurements

Cells were incubated with 3 μM fura-2 AM (Invitrogen) for 40 min at room temperature with gentle agitation. Fura-2 AM was dispensed from a 1 mM stock solution in DMSO containing 25% (wt/wt) pluronic F127 (BASF Corporation) that was stored at −20 C°. Cells were rinsed and recordings began after ∼20 min to allow time for de-esterification of the Ca^{2+} indicator. Since Fura-2 was loaded into cells as the AM ester, the cytoplasmic concentration of the indicator was not measured directly but was estimated based on measured changes in Ca^{2+} concentration after depolarization and repolarization (see below, Fig. 1). Culture dishes with adherent cells were placed on the stage of an inverted microscope (Nikon Diaphot TMD) and superfused continuously (∼5 ml/min) with normal Ringer's solution. Drug application was accomplished by changing the solution bathing individual cells (∼200 ms) using a system of microcapillaries (Drummond microcaps, 20 μl) mounted on a micromanipulator.

To measure $[Ca^{2+}]_i$, neurons were illuminated by light from a 150 W xenon lamp that was first passed through excitation filters (350 ± 5 nm, 380 ± 5 nm) mounted on a filter wheel rotating at 40–100 Hz and then focused with a 40× objective (Nikon, Fluor, NA 1.3). Emitted light passed through a long-pass dichroic mirror (400 nm) and emission filter (510 ± 10 nm) and was detected with a photomultiplier tube (Thorn EMI 9124). A spectrophotometer (Cairn Research Limited) was used to control the filter wheel and measure the spatially averaged fluorescence intensity at the two excitation wavelengths. Fluorescence measurements were made at 4–5 Hz and saved on a laboratory computer. $[Ca^{2+}]_i$ was calculated according to the method of

Grynkiewicz et al. (1985) as described previously (Colegrove et al., 2000a).

Voltage Clamp

Simultaneous measurements of depolarization-evoked $[Ca^{2+}]_i$ elevations and voltage-sensitive Ca^{2+} currents (I_{Ca}) were made under voltage clamp in fura-2 AM–loaded cells using the perforated patch technique. Patch electrodes (1–2 MΩ) were pulled (Sutter Instruments P-97) and tips were filled with a solution containing (in mM) 125 CsCl, 5 $MgCl_2$, 10 HEPES, and 0 or 6.5 mM Na^+ (the latter with equimolar reduction in CsCl), pH 7.3 with CsOH. After filling tips, pipettes were back-filled with the same solution supplemented with 520 μM amphotericin B, dispensed from concentrated aliquots (12 mg/100 μl DMSO). Fresh amphotericin B–containing internal solutions were made and kept on ice and used within 2 h. For the cells included in this study, after achieving a high resistance seal, series resistance declined over 5–10 min to <10 MΩ. Cells were exposed to an extracellular solution containing (in mM) 130 TEACl, 10 HEPES, 10 glucose, 2 $CaCl_2$, 1 $MgCl_2$, pH 7.3 with TEAOH. Currents were measured with an Axopatch 200A voltage clamp (Molecular Devices) using series resistance compensation (~90%) and were filtered at 5 kHz. Neurons were held at −70 mV and depolarized to voltages between −35 and −10 mV while current and fluorescence intensity were measured at 2–5 kHz just before (10–100 ms) and after (100–200 ms) changes in voltage, and at 4–5 Hz otherwise, and saved on a laboratory computer. Currents were corrected for a linear leak based on responses to small hyperpolarizing voltage steps. $[Ca^{2+}]_i$ elevations evoked under voltage clamp were somewhat larger than those elicited by high K^+ at comparable membrane potentials, presumably because of more rapid depolarization and more efficient Ca^{2+} channel activation under voltage clamp. However, $[Ca^{2+}]_i$ recovery kinetics after repolarization were similar for the two techniques.

Spatially Uniform Model

To investigate how depolarization-evoked $[Ca^{2+}]_i$ elevations are defined by the Ca^{2+} handling systems that operate in sympathetic neurons, we characterized these systems experimentally and obtained analytical expressions that described their activity. We then asked if these expressions, when used as the defining rate equations in a model of Ca^{2+} dynamics, make it possible to reconstruct observed depolarization-evoked $[Ca^{2+}]_i$ responses. We began with responses elicited under relatively simple experimental conditions in which all but a few transport pathways are blocked. Once an adequate description of $[Ca^{2+}]_i$ dynamics was in hand, we examined responses under conditions where additional transport mechanisms were enabled. At each stage, it was asked if the differences in evoked $[Ca^{2+}]_i$ responses observed after enabling a particular system can be understood in terms of the properties of that system in the functional context provided by the other systems. We began by incorporating the measured descriptions of Ca^{2+} handling into a spatially uniform model of Ca^{2+} dynamics, and asked if such a model can account for measured responses. We found that the uniform model was adequate to account for responses to weak depolarization, but not responses to strong depolarization, when intracellular Ca^{2+} gradients are expected to be steep. We then turned to a diffusion model that incorporated the same transport and buffering descriptions but considered spatially heterogeneous Ca^{2+} signals. Since the uniform and nonuniform models are similar, we give an overview of the uniform model here and describe the diffusion model in the Appendix.

The spatially uniform model includes three cellular compartments, cytoplasm, mitochondria, and the ER with free Ca^{2+} concentrations $[Ca^{2+}]_i$, $[Ca^{2+}]_{MT}$, and $[Ca^{2+}]_{ER}$, respectively. These dynamical variables change at a rate that depends on the intercompartmental net Ca^{2+} fluxes ($\tilde{J}_i$, $\tilde{J}_{MT}$, $\tilde{J}_{ER}$, e.g., in nmol/s) and volumes (v_i, v_{MT}, v_{ER}, e.g., in li) scaled by buffering factors (κ_i', κ_{MT}', κ_{ER}'):

$$\frac{d[Ca^{2+}]_i}{dt} = -\frac{\tilde{J}_i}{v_i\kappa_i'}$$

$$\frac{d[Ca^{2+}]_{MT}}{dt} = \frac{\tilde{J}_{MT}}{v_{MT}\kappa_{MT}'} \qquad \text{(M1)}$$

$$\frac{d[Ca^{2+}]_{ER}}{dt} = \frac{\tilde{J}_{ER}}{v_{ER}\kappa_{ER}'},$$

where

$$\tilde{J}_i = \tilde{J}_{PM} + \tilde{J}_{MT} + \tilde{J}_{ER} \qquad \text{(M2)}$$

and

$$\tilde{J}_{PM} = \tilde{J}_{VSCC} + \tilde{J}_{Extru}$$

$$\tilde{J}_{MT} = \tilde{J}_{uni} + \tilde{J}_{NaCa} \qquad \text{(M3)}$$

$$\tilde{J}_{ER} = \tilde{J}_{SERCA} + \tilde{J}_{Release}.$$

These equations can be rewritten so that they are more easily related to measured cytoplasmic Ca^{2+} fluxes:

$$\frac{d[Ca^{2+}]_i}{dt} = -J_i$$

$$\frac{d[Ca^{2+}]_{MT}}{dt} = J_{MT}\frac{v_i\kappa_i'}{v_{MT}\kappa_{MT}'} \qquad \text{(M4)}$$

$$\frac{d[Ca^{2+}]_{ER}}{dt} = J_{ER}\frac{v_i\kappa_i'}{v_{ER}\kappa_{ER}'},$$

where

$$J_i = \frac{\tilde{J}_i}{v_i\kappa_i'}$$

$$= \frac{\tilde{J}_{PM} + \tilde{J}_{MT} + \tilde{J}_{ER}}{v_i\kappa_i'} \qquad \text{(M5)}$$

$$= J_{PM} + J_{MT} + J_{ER}$$

and

$$J_{PM} = \frac{\tilde{J}_{PM}}{v_i\kappa_i'}$$

$$J_{MT} = \frac{\tilde{J}_{MT}}{v_i\kappa_i'} \qquad \text{(M6)}$$

$$J_{ER} = \frac{\tilde{J}_{ER}}{v_i\kappa_i'}.$$

These fluxes will be referred to as free Ca^{2+} fluxes. In the following, we describe how components of the model were characterized experimentally. The equations that were used to represent the fluxes are listed in the Appendix.

Dynamics of Cytoplasmic Total Ca Concentration

According to the spatially uniform model, Ca^{2+} is uniformly distributed within the cytoplasm at all times. Such a description is expected to provide a reasonable approximation to measured $[Ca^{2+}]$ responses as long as the rate of net Ca^{2+} transport between compartments is slow compared with the rate of Ca^{2+} diffusion within compartments. The cytoplasmic total Ca concentration $[Ca]_i$ changes at a rate that depends on both the net Ca flux into the cytoplasm ($\tilde{J}_i$) and the cytoplasmic volume (v_i):

$$\frac{d[Ca]_i}{dt} = -\frac{\tilde{J}_i}{v_i} = -\frac{\tilde{J}_i}{v_{Cell} f_i}, \tag{M7}$$

where, by convention, fluxes that lead to an increase in $[Ca]_i$ are negative. Cytoplasmic volume was taken as the product of total cell volume (v_{Cell}) estimated from the membrane capacitance (C_m), assuming a specific capacitance of 1 $\mu F/cm^2$, and the fraction (f_i) of the total cell volume occupied by cytoplasm. Since cells plated on polylysine-coated glass coverslips assumed an approximately spherical shape, we calculated v_{Cell} as $(1/6\sqrt{\pi})(C_m \times 10^{-6})^{3/2}$ cm^3. Sources of error in our estimate of v_i include deviations from spherical geometry and uncertainty in the precise value of f_i. We chose not to estimate f_i explicitly but instead to include it as a factor in the buffering parameters to be estimated. Errors in our estimate of v_i arising from deviations from spherical geometry would be expected to influence the estimated buffering parameters through their dependence on f_i (see below).

Dynamics of Cytoplasmic Free Ca Concentration

The free cytoplasmic Ca concentration ($[Ca^{2+}]_i$) changes at a rate that depends on the ratio of $\tilde{J}_i$ to the cytoplasmic volume scaled by a buffering factor (κ_i'):

$$\frac{d[Ca^{2+}]_i}{dt} = -\frac{\tilde{J}_i}{v_i \kappa_i'} = -\frac{\tilde{J}_i}{v_{Cell}(f_i \kappa_i')}, \tag{M8}$$

This uses the fast buffering approximation, according to which Ca^{2+} binding to buffers is fast compared with changes in $[Ca^{2+}]_i$. This is a reasonable approximation for fura-2, which achieves equilibrium binding to Ca^{2+} with a time constant that is <10 ms (Kao and Tsien, 1988), and the changes in $[Ca^{2+}]_i$ that we describe occur on a time scale of 100 ms to minutes. For the endogenous buffers, the approximation requires experimental validation. One approach to validating the fast buffer approximation is to calculate $[Ca^{2+}]_i$ trajectories using the approximation and then compare with measured responses.

Cytoplasmic Ca^{2+} Buffering

The quantity κ_i' is related to the well-known differential buffering factor κ_i and includes contributions from both endogenous (κ_{Endog}) and exogenous buffers (κ_{fura}):

$$\begin{aligned}\kappa_i' &= 1 + \kappa_i \\ &= 1 + \sum_j \frac{\partial [CaB_j]}{\partial [Ca^{2+}]_i} \\ &= 1 + \underbrace{\sum_j \frac{B_{total,j} K_{d,j}}{([Ca^{2+}]_i + K_{d,j})^2}}_{EndogenousBuffers} + \underbrace{\frac{B_{total,fura} K_{d,fura}}{([Ca^{2+}]_i + K_{d,fura})^2}}_{ExogenousBuffer} \\ &= 1 + \kappa_{Endog}([Ca^{2+}]_i) + \kappa_{Fura}([Ca^{2+}]_i),\end{aligned} \tag{M9}$$

where the j^{th} endogenous buffer is present at concentration $B_{total,j}$ and binds Ca^{2+} with dissociation constants $K_{d,j}$. In our experiments, the only exogenous buffer is fura-2, present at concentration $B_{total,fura}$ (estimated in different cells to be ~50–100 μM) with a dissociation constant $K_{d,fura}$ assumed to be 224 nM. Albrecht et al. (2002) provided a description of the $[Ca^{2+}]_i$ dependence of κ_i' in sympathetic neurons and estimates of κ_{Endog} and κ_{fura} near resting $[Ca^{2+}]_i$. In the following, we treat κ_{Endog} as a $[Ca^{2+}]_i$-independent constant to be determined, for example, describing contributions from low affinity endogenous buffers, and attribute the $[Ca^{2+}]_i$ dependence of κ_i' to fura-2. Accordingly, κ_i' depends on $[Ca^{2+}]_i$ in a way that can be described by two lumped parameters, $(1+\kappa_{Endog})$ and $B_{total,fura}$. However, since κ_i' appears in the equations describing $[Ca^{2+}]_i$ dynamics scaled by f_i (see Eq. M8 above), it is convenient to define the lumped parameters $P_1 = f_i(1 + \kappa_{Endog})$ and $P_2 = f_i B_{total,fura}$, which can be determined from measured quantities:

$$\begin{aligned}f_i \kappa_i' &= f_i\left(1 + \kappa_{Endog}\right) + \frac{f_i B_{total,fura} K_{d,fura}}{([Ca^{2+}]_i + K_{d,fura})^2} \\ &= P_1 + P_2\left[\frac{K_{d,fura}}{([Ca^{2+}]_i + K_{d,fura})^2}\right].\end{aligned} \tag{M10}$$

In the following, we drop the prime with the understanding that κ_i differs from the more common definition by unity. To estimate the two parameters P_1 and P_2, we obtained two independent measurements of $f_i\kappa_i$ at low and high $[Ca^{2+}]_i$ from the initial changes in $[Ca^{2+}]_i$ that follow depolarization and repolarization, respectively (Fig. 1). The first measurement of $f_i\kappa_i$ was made near resting $[Ca^{2+}]_i$ as the ratio of $I_{Ca}/2Fv_{Cell}$ to $-d[Ca^{2+}]_i/dt$ during the early phase of the response, when $[Ca^{2+}]_i$ increases approximately linearly with time. Since I_{Ca} is time dependent, we used the average of I_{Ca} over a short time interval that included the peak (at −35 mV, from 50 to 150 ms after the onset of depolarization; at −20 mV, from 3–51 ms after the onset of depolarization). The initial rate of rise of $[Ca^{2+}]_i$ ($d[Ca^{2+}]_i/dt$) was measured by fitting a line to the initial rising phase of the $[Ca^{2+}]_i$ response (−35 mV, during a 450-ms interval starting at the instant of depolarization; −10 mV, from 3–51 ms after depolarization onset). The second measurement of $f_i\kappa_i$ was obtained from the ratio of $I_{Ca}/2Fv_{Cell}$ to the instantaneous change in $-d[Ca^{2+}]_i/dt$ ($\Delta d[Ca^{2+}]_i/dt$) after repolarization (Fig. 1). Given the two estimates of $f_i\kappa_i$ near resting and peak $[Ca^{2+}]_i$, P_1 and P_2 were determined algebraically or by fitting the measurements with Eq. M10, which provided an initial characterization of the $[Ca^{2+}]_i$ dependence of $f_i\kappa_i$. However, since the two $f_i\kappa_i$ measurements from which P_1 and P_2 were determined included errors arising from I_{Ca} averaging and calculations of $d[Ca^{2+}]_i/dt$ from noisy $[Ca^{2+}]_i$ signals, and because they represent estimates of $f_i\kappa_i$ at only two values of $[Ca^{2+}]_i$, P_1 and P_2 were treated as initial

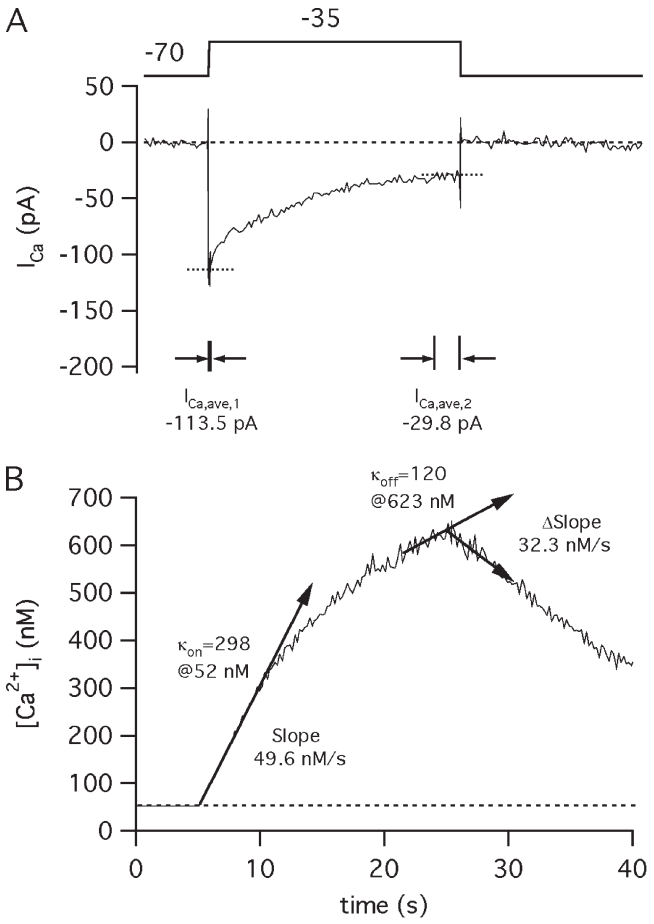

Figure 1. Method used to estimate cytoplasmic Ca^{2+} buffering strength. Buffering strength was characterized quantitatively based on measurements of I_{Ca} and changes in $[Ca^{2+}]_i$ that follow depolarization and repolarization. (A) Illustration of the Ca^{2+} current elicited by stepping the membrane potential from −70 to −35 mV. Dotted lines indicate average I_{Ca} during the intervals indicated by arrows. (B) $[Ca^{2+}]_i$ response elicited by this depolarization. Arrows indicate the initial rate of rise of $[Ca^{2+}]_i$ after depolarization, and the change in $d[Ca^{2+}]_i/dt$ after repolarization. These measurements were used to describe Ca^{2+} buffering strength near resting $[Ca^{2+}]_i$ (in this case 52 nM) and at the peak of the response (623 nM), which made it possible to estimate the two parameters P_1 and P_2 of $f_i\kappa_i$ according to Eq. M10.

estimates of the parameters of $f_i\kappa_i$, which were then optimized by fitting to measured responses.

Measuring Components of the Cytoplasmic Ca^{2+} Flux

In the following, the free cytoplasmic Ca^{2+} flux (J_i, e.g., in nM/s) represents the rate at which Ca^{2+} enters or leaves the cytoplasm ($\tilde{J}_i$, nmol/s) divided by $v_i\kappa_i$. Components of J_i representing different pathways were measured as follows. The component representing Ca^{2+} entry through voltage-sensitive Ca^{2+} channels (J_{VSCC}) was taken as the ratio of the associated net Ca^{2+} flux ($\tilde{J}_{VSCC} = I_{Ca}/2F$) and $v_i\kappa_i$, where F is the Faraday constant. The rate of Ca^{2+} extrusion across the plasma membrane (J_{Extru}) was measured as the total cytoplasmic Ca^{2+} flux ($-d[Ca^{2+}]_i/dt$) during the recovery after depolarization-induced $[Ca^{2+}]_i$ elevations in cells treated with carbonyl cyanide *p*-trifluoromethoxyphenylhydrazone (FCCP) and thapsigargin (Tg) to inhibit Ca^{2+} uptake by mitochondria and the ER, respectively (Colegrove et al., 2000a). J_{Extru} was described by Eqs. A4 and A5 (see Appendix). The rate of Ca^{2+} uptake by the mitochondrial Ca^{2+} uniporter (J_{uni}) was measured as the FCCP-sensitive component of the total flux under conditions where mitochondrial Ca^{2+} release via the Na/Ca exchanger was inhibited, either by using Na^+-free pipette solutions or treating cells with the specific Na/Ca exchange inhibitor CGP 37157 (CGP). Specifically, J_{uni} was measured by subtracting the FCCP-resistant flux ($J_{i,+FCCP}$) from the total flux at corresponding $[Ca^{2+}]_i$ levels during the recovery:

$$J_{uni}(t) = J_i(t) - J_{i,+FCCP}([Ca^{2+}]_i(t)) . \quad \text{(M11)}$$

This method follows from the idea that the total Ca^{2+} flux is the sum of an FCCP-sensitive flux (J_{uni}), and an FCCP-resistant flux ($J_{i,+FCCP} = J_{Extru}$) that depends on $[Ca^{2+}]_i$ at each time point during the recovery (Colegrove et al., 2000a). J_{uni} was described using Eqs. A11 and A12. The rate of Ca^{2+} release via the mitochondrial Na/Ca exchanger ($J_{Na/Ca}$) was measured as the CGP-sensitive component of the total Ca^{2+} flux in cells where the exchanger was enabled by including Na^+ in the pipette solution. $J_{Na/Ca}$ was determined by subtracting the CGP-resistant flux ($J_{i,+CGP}$) from the total flux at corresponding $[Ca^{2+}]_i$ levels during the recovery:

$$J_{Na/Ca}(t) = J_i(t) - J_{i,+CGP}([Ca^{2+}]_i(t)) . \quad \text{(M12)}$$

This makes use of the observation that $J_{i,+CGP}$ is a function of $[Ca^{2+}]_i$ at each time during the recovery (Colegrove et al., 2000a). J_{NaCa} was described using Eqs. A20–A22. Since Na^+ was included in the pipette solution in these experiments, it is possible that $J_{i,+CGP}$ contains a component representing Ca^{2+} entry via the plasma membrane Na/Ca exchanger (NCX) operating in reverse mode (external solutions were Na^+ free). Such a component would not interfere with our measurement of $J_{Na/Ca}$ as long as the rate of Ca^{2+} entry via NCX is a single-valued function of $[Ca^{2+}]_i$ at fixed membrane potential. This is expected based on the kinetic properties of NCX (Weber et al., 2001), assuming that in our experiments $[Na^+]_i$ is approximately constant. The rate of mitochondrial Ca^{2+} transport (J_{MT}) was measured as the FCCP-sensitive component of J_i in cells where mitochondrial uptake and release were both active. J_{MT} was determined by subtracting the FCCP-resistant flux ($J_{i,+FCCP}$) from the total flux at corresponding $[Ca^{2+}]_i$ levels during the recovery:

$$J_{MT}(t) = J_i(t) - J_{i,+FCCP}([Ca^{2+}]_i(t)) . \quad \text{(M13)}$$

Here, the FCCP-sensitive flux gives $J_{uni} + J_{NaCa}$ instead of only J_{uni} because the Na/Ca exchanger is enabled by including Na^+ in the pipette solutions. Finally, descriptions of ER Ca^{2+} uptake and release fluxes were taken from Albrecht et al. (2002).

Curve Fitting

Analysis was performed using IgorPro (Wavemetrics). Individual Ca^{2+} transport and buffering systems were described mathematically by fitting equations to measured quantities (see Appendix). While the equations were mechanistically motivated, they can be considered as empirical descriptions of the way the activity of each system depends on the corresponding independent variables. The differential equations were numerically integrated using the built-in IntegrateODE function in IgorPro (fourth order Runge-Kutta method with adaptive step size). In Cases 1 and 2, we fit the integrated responses by optimizing the two parameters (P_1, P_2) that describe cytoplasmic Ca^{2+} buffering. In the other cases, we examined how the agreement between calculated and simulated responses varied over a range of the parameter values

that were not completely constrained by experiment (e.g., diffusion coefficient of endogenous buffer, D_{Endog}, mitochondrial fractional volume, v_{MT}/v_{Cell}). To describe I_{Ca} during numerical integration, we used the measured leak-subtracted Ca^{2+} current during the period of depolarization, and zeroed the current at other times to avoid contributions from baseline current fluctuations and drift during the recovery, which occurred over hundreds of seconds. In fitting the equation for J_{Extru} to measurements from responses over a $[Ca^{2+}]_i$ range that did not extend far beyond ~300 nM, we constrained $EC_{50,Extru}$ to 350 nM, near the population average, and fit to obtain the remaining parameter values.

Drugs

CGP 37157 was a gift from Anna Suter (Novartis). Unless indicated otherwise, all other compounds were obtained from Sigma-Aldrich.

RESULTS

We measured depolarization-evoked $[Ca^{2+}]_i$ responses and Ca^{2+} currents simultaneously in fura-2 AM–loaded sympathetic neurons under voltage clamp, using the perforated patch technique to reduce disruption of the intracellular milieu. Neurons were depolarized from a holding potential of −70 mV to voltages ranging from −35 to −10 mV to stimulate Ca^{2+} entry through predominantly N-type Ca^{2+} channels (Jones and Mark, 1989) at different rates, and the resulting $[Ca^{2+}]_i$ responses were recorded. We examined five cases of increasing complexity. In each case, we compared measured $[Ca^{2+}]_i$ responses with calculated responses deduced from quantitative descriptions of Ca^{2+} transport and buffering obtained under the same experimental conditions, using the measured Ca^{2+} current to describe the rate of Ca^{2+} entry during the response. To minimize complications arising from cell-to-cell variability, we compared responses elicited in the simplest cases (Cases 1–3) in the same cells. While this required long and stable I_{Ca} and $[Ca^{2+}]_i$ recordings, it made it feasible to address the following questions. (a) Given a description of Ca^{2+} handling that accounts for $[Ca^{2+}]_i$ responses elicited by weak depolarization when Ca^{2+} uptake and release by internal stores is inhibited (Case 1), is it possible to account for responses elicited by the same stimulus when mitochondrial Ca^{2+} uptake is enabled (Case 2) by simply adding a functional description of the mitochondrial uniporter? (b) Does a description of Ca^{2+} handling that accounts for responses to weak depolarization also account for responses to strong depolarization if the larger Ca^{2+} current is used as the "input" in the calculations? After addressing Cases 1–3, we analyzed contributions from Ca^{2+} release by the mitochondrial Na/Ca exchanger (Case 4) and Ca^{2+} uptake and release by the ER (Case 5). Finally we compared published measurements of depolarization-induced changes in mitochondrial and ER total [Ca] levels with calculated changes deduced from the model incorporating all the measured Ca^{2+} handling systems.

Case 1. Cytoplasmic $[Ca^{2+}]$ Dynamics Regulated by Ca^{2+} Entry, Extrusion, and Buffering

We start with the simplest case in which $[Ca^{2+}]_i$ dynamics depend on the interplay between Ca^{2+} transport across the surface membrane and cytoplasmic Ca^{2+} buffering, without contributions from internal stores. For these measurements, cells were treated with FCCP (1 μM) and Tg (20–200 nM) to inhibit Ca^{2+} uptake by mitochondria and the ER, respectively. Fig. 2 (A and B) illustrates a representative response. Weak depolarization from −70 to −35 mV evoked a Ca^{2+} current (I_{Ca}; Fig. 2 A) that led to an increase in $[Ca^{2+}]_i$ from a resting level of ~60 nM to slightly over 600 nM. After repolarization, I_{Ca} underwent rapid deactivation and $[Ca^{2+}]_i$ recovered slowly toward its prestimulation level.

Measurement and Characterization of the Total Ca^{2+} Flux. To develop a quantitative description of Ca^{2+} dynamics, we characterized the Ca^{2+} handling systems that are expected to define how $[Ca^{2+}]_i$ changes during and after stimulated Ca^{2+} entry. It was then asked if these characterizations, when taken together, can account for the observed $[Ca^{2+}]_i$ responses.

The total cytoplasmic Ca^{2+} flux (J_i, nM/s) was measured throughout the response by calculating $-d[Ca^{2+}]_i/dt$ at each point in time. Assuming that (a) Ca^{2+} transport by stores is completely inhibited, (b) cytoplasmic Ca^{2+} is uniformly distributed, and that (c) Ca^{2+} binding to cytoplasmic buffers reaches equilibrium rapidly compared with $[Ca^{2+}]_i$ relaxations induced by Ca^{2+} entry, J_i has the following simple physical interpretation. It is the net flux of Ca^{2+} across the surface membrane per unit cytoplasmic volume scaled by a $[Ca^{2+}]_i$-dependent buffering factor (κ_i) that describes the relationship between changes in free and total Ca concentration (Eqs. M4 and M5). These fluxes will be referred to as "free Ca^{2+} fluxes" (e.g., in nM/s) and represented by J's, to distinguish them from the net Ca^{2+} fluxes representing the amount of Ca^{2+} transported per unit time, which will be designated by a tilde ($\tilde{J}$, e.g., in nmol/s).

Fig. 2 C plots J_i versus $[Ca^{2+}]_i$ throughout the response, distinguishing between the onset and recovery phases of the response. During the onset, J_i first increases rapidly to become a large inward flux (transition 1→2, see downward "On" arrow; note that inward fluxes are negative). J_i then hovers at ~−50 nM/s while $[Ca^{2+}]_i$ <200 nM before declining in magnitude during the remainder of the onset as $[Ca^{2+}]_i$ approaches its peak value (Point 3). After repolarization, J_i changes sign to become an outward flux (transition 3→4, see upward "Off" arrow) and then declines toward zero as $[Ca^{2+}]_i$ approaches its resting level (Point 5). We were

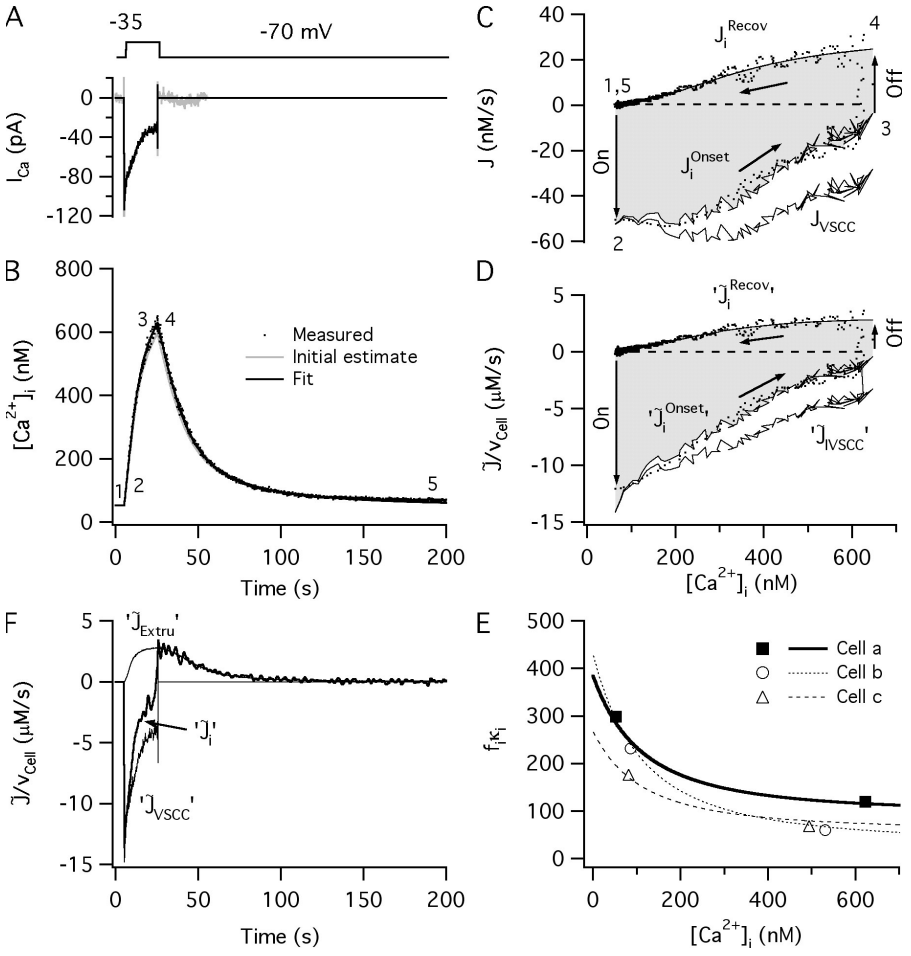

Figure 2. Analysis of a $[Ca^{2+}]_i$ response elicited by weak depolarization in the absence of Ca^{2+} uptake and release by internal stores (Case 1). (A) Depolarization-evoked Ca current I_{Ca}. (B) Measured $[Ca^{2+}]_i$ response (dots). Gray trace shows the result of integrating Eq. 2 using a description of $f_i\kappa_i$ derived from "on" and "off" responses obtained from the same cell. Dark trace shows integrated response after optimizing the parameters of $f_i\kappa_i$. Traces are nearly superimposable. (C) Measurement of total free Ca^{2+} flux during the response onset and recovery (J_i^{Onset}, J_i^{Recov}). Numbers refer to transition points between onset and recovery (see Results). Shaded region shows the contribution from Ca^{2+} entry (J_{VSCC}) to the free Ca^{2+} flux during the onset. (D) Measurement of (volume-normalized) net Ca^{2+} fluxes during the response onset and recovery. Shaded region shows the contribution from Ca^{2+} entry ($\tilde{J}_{VSCC}$) to the net flux during the onset. Net fluxes per unit cell volume are enclosed by quotes. (E) $[Ca^{2+}]_i$ dependence of Ca^{2+} buffering strength. Filled squares show measurements from the cell illustrated and the thick line shows the buffering curve calculated from Eq. M10 using parameters deduced by fitting the spatially uniform model to the $[Ca^{2+}]_i$ response in B. Open symbols and interrupted curves show measurements and calculations from two other cells under the same condition. (F) Comparison between the time course of the net Ca^{2+} flux underlying the dynamics of $[Ca^{2+}]_i$ (thick trace) and its components representing Ca^{2+} entry and extrusion (thin traces). Parameter values for this cell were as follows: $V_{max,Extru}$ = 30.3 nM/s, $K_{d,Extru}$ = 350 nM, n_{Extru} = 2.5, $f_i\kappa_{Endog}$ = 95.5, $f_iB_{total,Fura}$ = 64.7 μM, $k_{leak} = 1.3 \times 10^{-7}\ s^{-1}$.

unable to resolve the rapid changes in J_i that occur during the early moments of the onset and recovery that parallel I_{Ca} activation and deactivation, accounting for the apparent discontinuities in J_i between points 1,2, and 3,4.

Analysis of the Underlying Ca^{2+} Handling Systems. Inspection of Fig. 2 C shows that J_i declines during the onset between points 2 and 3. This is due to at least two factors. First, I_{Ca} undergoes partial inactivation (Fig. 2 A). Second, an outward flux develops as $[Ca^{2+}]_i$ rises, which reduces the impact of Ca^{2+} entry on $[Ca^{2+}]_i$. This flux is revealed after repolarization and I_{Ca} deactivation (Fig. 2 C, upward Off arrow) and is responsible for the subsequent $[Ca^{2+}]_i$ recovery. It represents the activity of all Ca^{2+} extrusion systems that operate during the recovery (Herrington et al., 1996; Wennemuth et al., 2003), including plasma membrane Ca^{2+} ATPase (PMCA), as well as a Ca^{2+} leak. Contributions from the plasma membrane Na/Ca exchanger are minimal because internal and external solutions are Na^+ free. This flux, which will be referred to as J_{Extru}, is given by the rate at which $[Ca^{2+}]_i$ declines during the recovery:

$$\left.\frac{d[Ca^{2+}]_i(t)}{dt}\right|_{Recov} = -J_i^{Recov}(t) = -J_{Extru}\left([Ca^{2+}]_i(t)\right). \quad (1)$$

Our previous work has shown that during the recovery, J_{Extru} depends solely on $[Ca^{2+}]_i$, indicating that the underlying Ca^{2+} transport systems adjust rapidly to changes in $[Ca^{2+}]_i$. Fig. 2 C (top, smooth curve) illustrates the $[Ca^{2+}]_i$ dependence of J_{Extru}.

We hypothesized that during the response, J_i is the sum of two flux components, voltage-sensitive Ca^{2+} entry (J_{VSCC}) and J_{Extru}. According to this idea, J_i is influenced by both J_{VSCC} and J_{Extru} during depolarization, but only J_{Extru} during the recovery (or rather that portion of the recovery after complete Ca^{2+} channel deactivation, when $J_{VSCC} = 0$). Extending our description of $[Ca^{2+}]_i$

dynamics to include the period of depolarization, and describing cytoplasmic Ca^{2+} buffering as in Materials and methods, we have

$$\frac{d[Ca^{2+}]_i(t)}{dt} = -J_i(t)$$

$$= -[J_{VSCC}(t) + J_{Extru}(t)] \quad (2)$$

$$= -\left[\frac{I_{Ca}(t)}{2Fv_{Cell}f_i\kappa_i\left([Ca^{2+}]_i(t)\right)} + J_{Extru}\left([Ca^{2+}]_i(t)\right)\right].$$

Reconstruction of the $[Ca^{2+}]_i$ Response. We reasoned that if J_{Extru} has the same $[Ca^{2+}]_i$ dependence during depolarization as it does during the recovery, then measurement of J_{Extru} during the recovery will provide a reliable description of Ca^{2+} removal during depolarization. In this case, it should be possible to reconstruct the entire $[Ca^{2+}]_i$ response by numerically integrating Eq. 2 subject to the initial condition:

$$[Ca^{2+}]_i(0) = [Ca^{2+}]_{i,rest}, \quad (3)$$

using the measured current as a time-dependent input to describe the rate of voltage-sensitive Ca^{2+} entry at each point in time.

To describe the $[Ca^{2+}]_i$ dependence of J_{Extru}, we used a look-up table consisting of the flux measurements at each $[Ca^{2+}]_i$, using linear interpolation to obtain values at each time step during numerical integration, or alternatively a smooth curve fit to the measurements based on Eqs. A4, and A5 (Fig. 2 C). These approaches gave essentially identical results. To describe the $[Ca^{2+}]_i$ dependence of $f_i\kappa_i$, we used On and Off responses to estimate the strength of Ca^{2+} buffering at low and high $[Ca^{2+}]_i$ (Fig. 1) and used these measurements to obtain initial estimates of the two parameters of $f_i\kappa_i$ (P_1, P_2) (see Eq. M10).

Using these descriptions of Ca^{2+} entry, extrusion, and buffering, we found that numerical integration of Eq. 2 provided a remarkably good description of the $[Ca^{2+}]_i$ response, both during the onset and the recovery, without any free parameters (Fig. 2 B, gray trace). Since the $[Ca^{2+}]_i$ dependence of $f_i\kappa_i$ is based on measurements at only two $[Ca^{2+}]_i$ levels (near resting and peak $[Ca^{2+}]_i$), we asked if a better approximation of the $[Ca^{2+}]_i$ response could be obtained by fitting the response, treating P_1 and P_2 as adjustable parameters. It was found that after fitting, the integrated response even more closely approximated the measured one (Fig. 2 B, dark trace). Moreover, the $[Ca^{2+}]_i$ dependence of $f_i\kappa_i$ calculated based on the optimized values of P_1 and P_2 was consistent with the initial estimates obtained from analysis of the On and Off responses (Fig. 2 E, compare thick curve with filled squares). The same analysis was performed on three cells stimulated with the same protocol, yielding similar results (Fig. 2 E). For these cells, the parameter values describing extrusion and buffering were $V_{max,Extru}$ = 29.8 ± 1.5 nM/s, n_{Extru} = 3.0 ± 0.3, $f_i\kappa_{Endog}$ = 63.0 ± 18.0, and $f_iB_{total,Fura}$ = 66.4 ± 12.2 μM.

What conclusions can be drawn from these results? While reconstruction of the $[Ca^{2+}]_i$ recovery follows trivially from the description of J_{Extru} as $-d[Ca^{2+}]_i/dt$ and the value of $[Ca^{2+}]_i$ at the instant of repolarization, reconstruction of the response onset does not. The description of J_{Extru} was obtained from analysis of the recovery, when the membrane potential was clamped at −70 mV, while during the onset V_m = −35 mV. This indicates that the description of J_{Extru} obtained from analysis of the recovery is also adequate to describe Ca^{2+} extrusion during the onset when the membrane potential is depolarized. Thus, the Ca^{2+} extrusion systems that are responsible for restoring $[Ca^{2+}]_i$ in the aftermath of depolarization do not appear to be strongly voltage dependent, at least over the range −70 to −35 mV. Moreover, the results are consistent with the idea that for a given (spatially averaged) $[Ca^{2+}]_i$ level, these systems generate a similar Ca^{2+} flux during the onset and recovery, as if the submembrane $[Ca^{2+}]_i$ levels that regulate extrusion during these phases of the response are comparable.

Properties of the Ca^{2+} Flux Components. Having validated our description of Ca^{2+} dynamics in Case 1, it is possible to obtain a description of the component of J_i representing Ca^{2+} entry during the response onset. This component (J_{VSCC}) can be calculated by subtracting J_{Extru} from J_i at corresponding values of $[Ca^{2+}]_i$ (Fig. 2 C, top, shaded region and bottom trace), which follows directly from the description of J_i as the sum of J_{VSCC} and J_{Extru} and the functional dependence of J_{Extru} on $[Ca^{2+}]_i$. After depolarization, J_{VSCC} undergoes a rapid increase in magnitude when it dominates J_i (Fig. 2 C, transition 1 2), which is followed by a secondary increase before declining to ~–30 nM/s as $[Ca^{2+}]_i$ approaches its peak value. The secondary increase might seem paradoxical, given that it occurs while I_{Ca} inactivates. However, since J_{VSCC} depends on the rate Ca^{2+} entry and the strength of Ca^{2+} buffering (Fig. 2 E), it is necessary to consider both sources of variation when evaluating changes in this flux during the onset.

Given measurements of the free Ca^{2+} fluxes and the $[Ca^{2+}]_i$ dependence of $f_i\kappa_i$, the net Ca^{2+} fluxes can be obtained by multiplying the free Ca^{2+} fluxes by $f_i\kappa_i$ at corresponding values of $[Ca^{2+}]_i$. The resulting fluxes are normalized by cell volume (not cytoplasmic volume, see Eq. M8) and will be designated by quotes to distinguish them from the un-normalized net fluxes. Fig. 2 D shows the volume-normalized net Ca^{2+} fluxes corresponding to the free Ca^{2+} fluxes in Fig. 2 C. These fluxes are larger in magnitude than the free Ca^{2+} fluxes

(note difference in the scale, μM/s vs. nM/s) and show a different dependence on $[Ca^{2+}]_i$. Most notably, after their initial rapid increase following depolarization, $\tilde{J}_i$ and $\tilde{J}_{VSCC}$ both decay monotonically, in contrast to the free Ca^{2+} fluxes. Therefore, J_{VSCC} does not parallel I_{Ca} during the response onset because it is the ratio of two declining quantities, $\tilde{J}_{VSCC}$ and $f_i\kappa_i$, with the latter falling more rapidly than the former. This relationship between the time dependence of $\tilde{J}_{VSCC}$ and the $[Ca^{2+}]_i$ dependence of $f_i\kappa_i$ is important, because it ultimately determines how $[Ca^{2+}]_i$ changes in response to depolarization.

Fig. 2 F shows how the net Ca^{2+} fluxes vary with time, illustrating how the rate of net Ca^{2+} transport depends continuously on the relative rates of Ca^{2+} entry and extrusion. Comparing plots of the net fluxes vs. $[Ca^{2+}]_i$ (Fig. 2 D) and time (Fig. 2 F) also illustrates an important difference between the independent variables that control the components of $\tilde{J}_i$. $\tilde{J}_{VSCC}$ is a function of time, expressing the time dependence of I_{Ca} at constant voltage, while $\tilde{J}_{Extru}$ is a function of $[Ca^{2+}]_i$ that varies because $[Ca^{2+}]_i$ is dynamic. $\tilde{J}_{VSCC}$ may also depend on $[Ca^{2+}]_i$, e.g., through $[Ca^{2+}]_i$-dependent modulation of N-type Ca^{2+} channel activity (Liang et al., 2003), but it is not necessary to explicitly include such effects in our description of Ca^{2+} entry since their impact is included in the direct measurements of $I_{Ca}(t)$.

These results demonstrate that in the absence of Ca^{2+} uptake and release by internal stores, $[Ca^{2+}]_i$ responses elicited by weak depolarization can be accurately described by a spatially uniform system endowed with $[Ca^{2+}]_i$-dependent Ca^{2+} extrusion and buffering mechanisms subject to time-dependent Ca^{2+} entry.

Case 2. Contributions from the Mitochondrial Ca^{2+} Uniporter during Weak Depolarization

This section describes the added contribution of the mitochondrial Ca^{2+} uniporter to depolarization-evoked $[Ca^{2+}]_i$ responses, using the same depolarization protocol as in the preceding section. Qualitatively, mitochondrial Ca^{2+} uptake is expected to increase the rate of cytoplasmic Ca^{2+} removal to an extent that increases steeply with $[Ca^{2+}]_i$. To study this directly, the same cells that were depolarized in the presence of FCCP were also stimulated in its absence to enable the uniporter. Since these cells were voltage clamped using a pipette solution that contained no added Na^+, the FCCP-sensitive flux provides a description of Ca^{2+} uptake via the uniporter, without contamination from the Na/Ca exchanger, which requires internal Na^+ for its operation.

Fig. 3 (A and B) illustrates a response elicited under these conditions from the same cell described in Fig. 2 before it was exposed to FCCP. While the Ca^{2+} current elicited by the voltage step was very similar to that observed in the presence of FCCP (compare dark and light traces in Fig. 3 A), $[Ca^{2+}]_i$ increased more slowly during the onset, showed a smaller peak, and recovered faster, consistent with the expected effects of enabling mitochondrial Ca^{2+} uptake.

To investigate the free cytoplasmic Ca^{2+} flux during this response, we again calculated $J_i = -d[Ca^{2+}]_i/dt$ during the onset and recovery (Fig. 3 C). As in Case 1, J_i showed an initial rapid increase in magnitude followed by a slow secondary rise and ultimately a decline toward zero as $[Ca^{2+}]_i$ approached a steady elevated level (Point 3). After repolarization and I_{Ca} deactivation, J_i changed sign to become an outward flux, which then declined toward zero as $[Ca^{2+}]_i$ approached its resting level.

Analysis of the Ca^{2+} Handling Systems. Our previous work has shown that the decline in $[Ca^{2+}]_i$ during the recovery under these conditions of stimulation is influenced by the combined actions of Ca^{2+} extrusion and mitochondrial Ca^{2+} uptake by the uniporter (Colegrove et al., 2000a). Like J_{Extru}, the rate of Ca^{2+} uptake by the uniporter (J_{uni}) depends on $[Ca^{2+}]_i$ but not its history. Therefore, since both components of the free Ca^{2+} flux are defined by $[Ca^{2+}]_i$, so is their sum:

$$\left.\frac{d[Ca^{2+}]_i(t)}{dt}\right|_{Recov} = -J_i^{Recov}(t) = -\left[J_{Extru}\left([Ca^{2+}]_i(t)\right) + J_{uni}\left([Ca^{2+}]_i(t)\right)\right]\Big|_{Recov}. \quad (4)$$

(see Fig. 3 C). Extending this description to include the period of depolarization, we have

$$\frac{d[Ca^{2+}]_i(t)}{dt} = -\left[\frac{I_{Ca}(t)}{2Fv_{Cell}f_i\kappa_i\left([Ca^{2+}]_i(t)\right)} + \left[J_{Extru}\left([Ca^{2+}]_i(t)\right) + J_{uni}\left([Ca^{2+}]_i(t)\right)\right]\right], \quad (5)$$

subject to initial condition (Eq. 3).

Reconstruction of the $[Ca^{2+}]_i$ Response. To determine if Eq. 5 accurately describes $[Ca^{2+}]_i$ dynamics when mitochondrial Ca^{2+} uptake is enabled, we integrated this equation and compared the results with measured responses. The $[Ca^{2+}]_i$ dependence of $J_{Extru}+J_{uni}$ was described using a look-up table as in Case 1, or by fitting an equation to the J_i measurements during the recovery (Fig. 3 C). For fitting, the same equation and parameters were used for J_{Extru} as in Case 1 and J_{uni} was described using Eq. A12. We started with the characterization of Ca^{2+} buffering obtained from the same cell in the presence of FCCP, since the measured strength of Ca^{2+} buffering was similar in the two cases (Fig. 3 E, compare filled and open squares). With these descriptions of

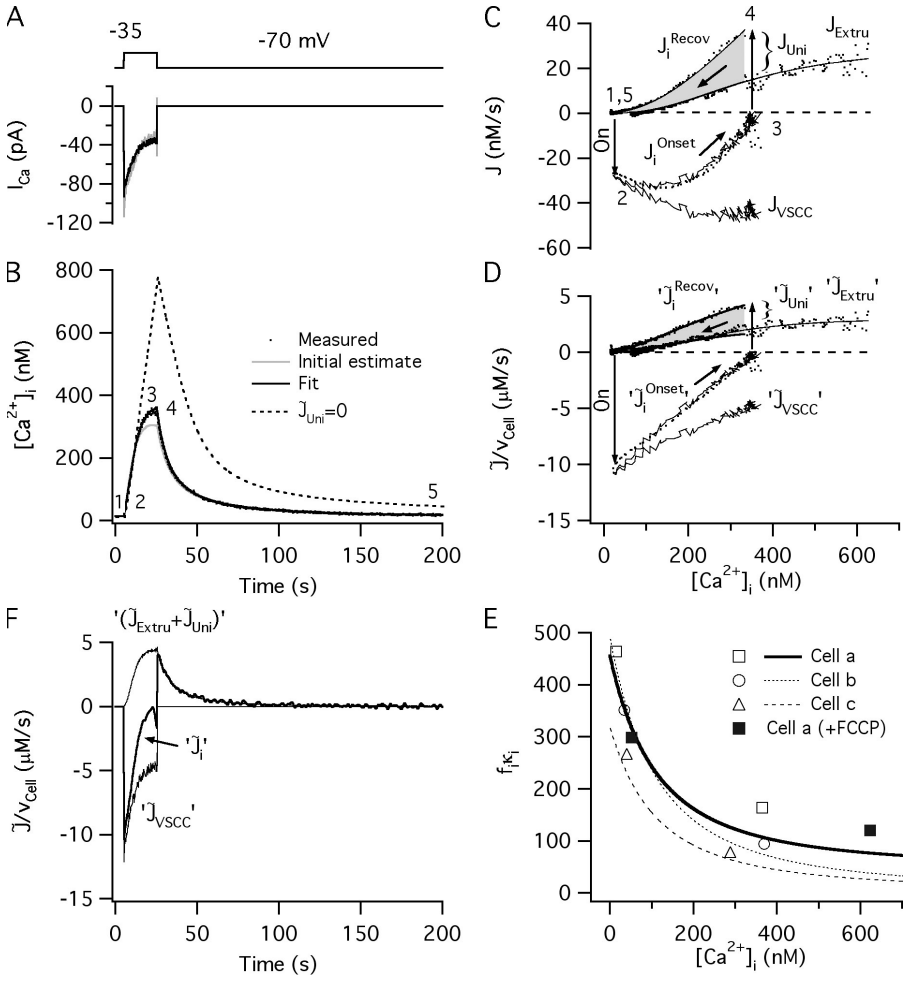

Figure 3. Analysis of Ca^{2+} responses elicited by weak depolarization when mitochondrial Ca^{2+} uptake is enabled (Case 2). (A) Depolarization-evoked Ca current I_{Ca} (dark trace; light trace shows I_{Ca} from Case 1 response for comparison). (B) $[Ca^{2+}]_i$ response (dots). Gray trace shows integrated form of Eq. 5 based on initial description of $f_i\kappa_i$ (E, open squares). Dark trace shows integrated results with optimized buffering parameters; dots and dark trace overlap. Dashed trace shows the result of integrating after setting $J_{uni} = 0$. (C) Measurement of the free Ca^{2+} fluxes during the response onset and recovery and their components. Shaded region shows contribution from the Ca^{2+} uniporter (J_{uni}) during the recovery. (D) Measurement of net Ca^{2+} fluxes during the response onset and recovery and their components. Shaded region shows contribution from the Ca^{2+} uniporter during the recovery. Single quotes designate net fluxes per unit cell volume. (E) $[Ca^{2+}]_i$ dependence of Ca^{2+} buffering strength. Open squares show measurements for the cell illustrated and the buffering curve calculated based on fitting the spatially uniform model to the $[Ca^{2+}]_i$ response in B. Open circles and triangles and interrupted curves show analogous measurements and calculations from two other cells. Filled squares show measurements from the same cell in the presence of FCCP. (F) Comparison between the time course of the net Ca^{2+} flux underlying the dynamics of $[Ca^{2+}]_i$ (thick trace) and its component representing Ca^{2+} entry and removal (thin traces). Parameter values for the calculated response: $f_i\kappa_{Endog} = 48.2$, $f_iB_{total,Fura} = 91.2$ μM, $k_{leak} = 1.3 \times 10^{-7}$ s^{-1}, $A = 7.8 \times 10^{-4}$, $n_{uni} = 0.8$. J_{PMCA} parameters were the same as in Case 1.

Ca^{2+} handling, we found that the calculated response closely resembled the measured response (Fig. 3 B, compare gray trace with dots), although it underestimated the $[Ca^{2+}]_i$ measurements during the period of depolarization. After optimizing the buffering parameters, the integrated $[Ca^{2+}]_i$ response was essentially indistinguishable from the measured one (Fig. 3 B, dark trace), and the $[Ca^{2+}]_i$ dependence of f_ik_i (Fig. 3 E, thick curve) was consistent with the measured values in the presence and absence of FCCP. The same comparison between responses elicited in the presence and absence of FCCP was performed in two other cells, giving comparable results (Fig. 3 E). Analysis of four additional cells stimulated under Case 2 conditions gave similar results. Overall, for these seven cells $f_i\kappa_{Endog} = 53.9 \pm 10.2$, $f_iB_{total,Fura} = 65 \pm 13$ μM, $A = 4 \pm 2 \times 10^{-4}$, and $n_{uni} = 1.0 \pm 0.2$.

Properties of the Ca^{2+} Flux Components. Analysis of the Ca^{2+} flux components (Fig. 3 C) shows how J_{VSCC} varies with $[Ca^{2+}]_i$ during the response onset. J_{VSCC} increases rapidly after depolarization (Fig. 3 C, top, transition 1 2) when it dominates J_i, and continues to increase despite inactivation of I_{Ca}. As in Case 1, this occurs because there are quantitative differences in the way I_{Ca} and $f_i\kappa_i$ change during the onset. While I_{Ca} shows a time course that is very similar to that observed in the presence of FCCP, $f_i\kappa_i$ changes more dramatically because $[Ca^{2+}]_i$ is restricted to a lower range, where $f_i\kappa_i$ is more sensitive to $[Ca^{2+}]_i$. As a result, the ratio $I_{Ca}/f_i\kappa_i$ increases throughout the onset, despite the decline in I_{Ca} due to inactivation. This complex behavior in not observed with the (volume-normalized) net Ca^{2+} fluxes obtained by multiplying the free Ca^{2+} fluxes by $f_i\kappa_i$ at corresponding $[Ca^{2+}]_i$ levels (Fig. 3 D). In particular, both $\tilde{J}_i$ and $\tilde{J}_{VSCC}$ decline monotonically as $[Ca^{2+}]_i$ rises throughout the depolarization (Fig. 3 D).

Perhaps the most striking difference observed when $[Ca^{2+}]_i$ responses are elicited while mitochondrial Ca^{2+} uptake is enabled is that $[Ca^{2+}]_i$ elevations are smaller and rates of Ca^{2+} removal are higher at all $[Ca^{2+}]_i$ levels. For example, when mitochondrial Ca^{2+} uptake is

enabled, the rate of net Ca^{2+} removal after repolarization, when $[Ca^{2+}]_i$ ~350 nM, exceeds 4 μM/s, roughly twice the rate observed at the corresponding $[Ca^{2+}]_i$ level when mitochondrial Ca^{2+} uptake is disabled (Fig. 2 D and Fig. 3 D). In addition, when the uniporter is enabled, Ca^{2+} entry and removal rates are in balance when $[Ca^{2+}]_i$ reaches a much lower level than that attained during depolarization in Case 1. When this same $[Ca^{2+}]_i$ level is reached in Case 1 (Fig. 2), there is still a large imbalance between Ca^{2+} entry and extrusion rates that favors a continued rise in $[Ca^{2+}]_i$. Mitochondrial Ca^{2+} uptake is not expected to influence steady-state $[Ca^{2+}]_i$ elevations when Ca^{2+} release by the Na/Ca exchanger is enabled and operates at less than its maximal rate. However, when release is inhibited, or saturated after a large Ca^{2+} load, mitochondria are expected to behave as "absorbing" organelles that depress $[Ca^{2+}]_i$. Consistent with this idea, we found that in three cells with low internal Na^+, which would be expected to promote continuous mitochondrial Ca^{2+} uptake, exposure to FCCP increased resting $[Ca^{2+}]_i$ (unpublished data). In intact cells with normal $[Na^+]_i$, this is not observed (Friel and Tsien, 1994).

We quantified the rate of mitochondrial Ca^{2+} uptake via the uniporter (J_{uni}) at each point in time (t) during the recovery by subtracting from the total flux $J_i(t)$ the FCCP-resistant flux evaluated at $[Ca^{2+}]_i(t)$ (Eq. M11). This flux component is illustrated by the shaded region in Fig. 3 C; the corresponding (volume-normalized) net Ca^{2+} flux is shown in panel D. Fig. 3 F compares the time courses of $\tilde{J}_{VSCC}$ and $\tilde{J}_{Extru} + \tilde{J}_{uni}$ (thin traces) and their sum $\tilde{J}_i$ (thick trace) throughout the response. As in Case 1, $\tilde{J}_i$ depends on the imbalance between Ca^{2+} entry and removal rates, the former depending explicitly on time (through the time dependence of I_{Ca}), the latter depending on $[Ca^{2+}]_i$ (through the $[Ca^{2+}]_i$ dependence of Ca^{2+} removal rates and buffering strength).

It should be noted that previous work suggests that mitochondrial Ca^{2+} uptake does not influence $[Ca^{2+}]_i$ dynamics appreciably when stimuli are weak and $[Ca^{2+}]_i$ is low (Thayer and Miller, 1990; Friel and Tsien, 1994). However, comparison of Figs. 2 and 3 shows that $[Ca^{2+}]_i$ responses elicited by weak depolarization were considerably larger when mitochondrial Ca^{2+} uptake is inhibited. Two factors contribute to this difference. First, our previous results indicate that FCCP has little effect on $[Ca^{2+}]_i$ responses in intact sympathetic neurons when $[Ca^{2+}]_i \leq$ ~200 nM (Friel and Tsien, 1994), a lower range than that achieved by 20-s depolarization to −35 mV under voltage clamp, which exceeds 350 nM. Second, the responses described here were elicited in cells with low internal Na^+. By suppressing Na^+-dependent mitochondrial Ca^{2+} release, this would leave uptake unopposed, increasing the overall rate of mitochondrial Ca^{2+} accumulation and exaggerating the difference between responses elicited in the presence and absence of FCCP.

Another way to illustrate the impact of the uniporter on $[Ca^{2+}]_i$ responses evoked by weak depolarization is to integrate Eq. 5 after setting A = 0 in Eq. A12 to eliminate contributions from the uniporter in the calculations. This produced a response (Fig. 3 B, dashed trace) that was very similar to that observed in the presence of FCCP (Fig. 2 B), the small differences being accounted for by differences in I_{Ca}, resting $[Ca^{2+}]_i$, and buffering strength (unpublished data).

Case 3. $[Ca^{2+}]_i$ Responses Elicited by Strong Depolarization

We next asked if the Ca^{2+} handling systems that define responses to weak depolarization in the preceding case can also account for $[Ca^{2+}]_i$ elevations elicited by strong depolarization. To examine this, cells were depolarized for 2–3 s from −70 to −10 mV. A response elicited by such a stimulus in the same cell examined in Cases 1 and 2 above is presented in Fig. 4 (A and B). The most obvious differences are the larger Ca^{2+} current (peak ~−3.3 nA) and $[Ca^{2+}]_i$ elevation (~1 μM). Two observations indicate that responses like those shown in Fig. 4 B are within the dynamic range of fura-2. First, larger $[Ca^{2+}]_i$ elevations were observed after exposure to FCCP (unpublished data). Second, measurements in other cells showed that stronger depolarizations produce even larger $[Ca^{2+}]_i$ responses (Fig. 4 F).

Fig. 4 C shows J_i calculated during the onset and recovery phases of the response. Qualitatively, J_i changes during depolarization and after repolarization as with the weaker stimuli in Cases 1 and 2 (see Fig. 2 C and Fig. 3 C). However, the magnitude of the flux is much larger. We asked if the same equation (Eq. 5) that describes cytoplasmic Ca^{2+} handling in Case 2 can also describe $[Ca^{2+}]_i$ responses elicited by stronger depolarization if the larger Ca^{2+} current is used as the time-dependent input. As in Case 2, measurements of J_i during the recovery were used to characterize the overall rate of Ca^{2+} removal (Fig. 4 C). Panel D shows the region enclosed by the dashed box in panel C on an expanded scale. The rate of Ca^{2+} removal increases steeply with $[Ca^{2+}]_i$, and shows a $[Ca^{2+}]_i$ dependence very similar to that observed after weak depolarization over the common range of $[Ca^{2+}]_i$ (open symbols).

Analysis of the Underlying Ca^{2+} Handling Systems. We measured the component of J_i representing Ca^{2+} uptake by the uniporter by subtracting J_{Extru} from J_i at corresponding values of $[Ca^{2+}]_i$ (shaded region in Fig. 4 D) and described the $[Ca^{2+}]_i$ dependence of J_{uni} using Eq. A12. Based on analysis of three cells, $A = 5.6 \pm 2.8 \times 10^{-6}$ and $n_{uni} = 1.8 \pm 0.2$, which is somewhat different from the parameter values obtained by fitting over the lower range of $[Ca^{2+}]_i$ in Case 2 (see Appendix). Measurements of

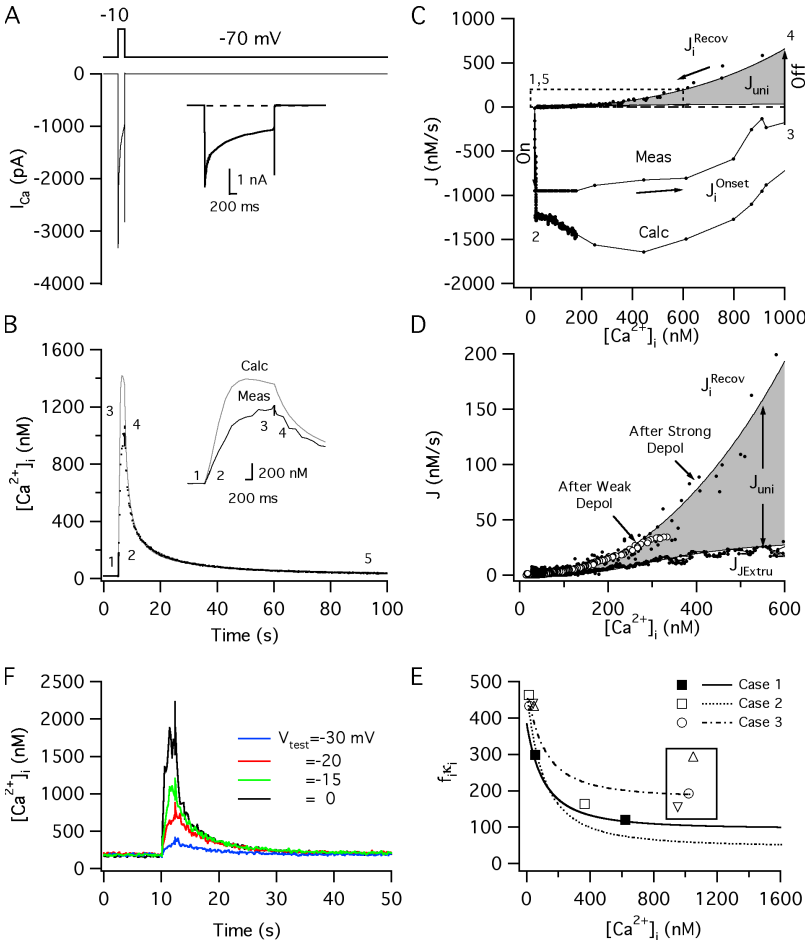

Figure 4. Analysis of Ca^{2+} responses elicited by strong depolarization when mitochondrial Ca^{2+} uptake is enabled (Case 3): spatially uniform model. A. Depolarization-evoked Ca current, I_{Ca}. (B) $[Ca^{2+}]_i$ response (dots). Gray trace shows integration of Eq. 5 based on description of $f_i\kappa_i$ from On and Off measurements in Case 1 from the same cell (filled squares, E). Parameter values for the calculated response: $A = 10^{-5}$, $n_{uni} = 1.6$. J_{PMCA} and buffering parameters were the same as in Case 1. Calculations of J_{Extru} and J_{uni} at $[Ca^{2+}]_i$ levels above the measured peak were based on extrapolations of the flux curves to higher levels. Insets in A and B show I_{Ca} and $[Ca^{2+}]_i$ during depolarization on an expanded scale. (C) Measurement of the free Ca^{2+} flux during the response onset and recovery. Shaded region shows contribution from the Ca^{2+} uniporter during the recovery (J_{uni}). (D) $[Ca^{2+}]_i$ dependence of the fluxes from C (dashed box) shown on an expanded scale. Measurements of J_i during the recovery overlap measurements from the same cell after weak depolarization (compare filled and open circles). (E) $[Ca^{2+}]_i$ dependence of Ca^{2+} buffering strength in Cases 1–3 from this cell. Open circles show measurements derived from the response shown in A and B. Triangles show measurements from two other cells studied with the same protocol. While measurements at low $[Ca^{2+}]_i$ agree with those from the same cell in Cases 1 and 2, the measurements at high $[Ca^{2+}]_i$ deviate systematically from extrapolated curves deduced from responses to weak depolarization. (F) $[Ca^{2+}]_i$ responses from another cell elicited by 2-s-long depolarizing pulses of different magnitudes, illustrating the dynamic range of the fura-2 measurements.

Ca^{2+} buffering strength near resting $[Ca^{2+}]_i$ were consistent with analysis of the same cell during weak depolarization in Cases 1 and 2 (Fig. 4 E), even though the rate of Ca^{2+} entry was >10 times higher. However, the apparent buffering strength measured at high $[Ca^{2+}]_i$ levels was approximately twofold higher than would be predicted based on extrapolations of the f_ik_i curve deduced from responses to weak depolarization. Although these estimates of buffering strength are derived from noisy measurements, a similar discrepancy was seen in each of the three cells studied in Cases 1–3 (Fig. 4 E, see box). This contrasts with the tightly clustered values of buffering strength near resting $[Ca^{2+}]_i$ measured from On responses to strong depolarization.

Comparison between Measured Responses and Calculations Based on the Spatially Uniform Model. Calculations based on Eq. 5 were performed using the Ca^{2+} buffering parameters obtained from the same cells under Case 1 conditions, reasoning that buffering strength should be similar, at least for overlapping ranges of $[Ca^{2+}]_i$. While the simulated responses closely paralleled the measured $[Ca^{2+}]_i$ responses during the recovery, as they must, given the way Ca^{2+} removal rate is defined in Eq. 5, the calculated values of $[Ca^{2+}]_i$ during depolarization were much larger than the measured ones (Fig. 4 B, compare continuous trace with dots). This was paralleled by a nearly twofold overestimation of J_i during the onset (Fig. 4 C, bottom traces). As shown above, this difference cannot be accounted for by fura-2 saturation (Fig. 4 F). Overall, we were unable to find a simple description of $f_i\kappa_i$ that made it possible to reconstruct $[Ca^{2+}]_i$ responses elicited by strong depolarization that also agreed with measurements obtained from responses elicited by weak depolarization. Therefore, we considered alternative explanations of the systematic difference between measured and calculated $[Ca^{2+}]_i$ during strong depolarization.

Reconstruction of the $[Ca^{2+}]_i$ Response Using a Diffusion Model. One possibility is that, in contrast to weak depolarization, the rate of Ca^{2+} entry during strong depolarization is sufficiently high compared with the rate of radial diffusion that $[Ca^{2+}]_i$ levels beneath the plasma membrane greatly exceed the spatial average. This would cause Ca^{2+} removal rates to be higher than expected

based on spatially averaged $[Ca^{2+}]_i$ levels. While this would be expected to include a higher rate of Ca^{2+} extrusion, the increase in J_{Extru} required to account for the upward shift in J_i during the onset (Fig. 4 C) is >25 times larger than the estimated maximal rate of extrusion. Increased mitochondrial Ca^{2+} uptake is more likely to play an important role. Given the steep $[Ca^{2+}]$ dependence of Ca^{2+} uptake by the uniporter, large increases in $[Ca^{2+}]_i$ in outer cytoplasmic shells would lead to disproportionately higher rates of mitochondrial Ca^{2+} uptake in those same shells. Indeed, measurements of total mitochondrial Ca concentration indicate that this occurs (Pivovarova et al., 1999; Hongpaisan et al., 2001; see below). One consequence would be that a larger fraction of the Ca^{2+} that enters the cytoplasm during depolarization would be taken up by peripheral mitochondria than expected based on the magnitude of spatially averaged $[Ca^{2+}]_i$. As a result, a smaller fraction of the Ca^{2+} that enters the cell would be available to bind fura-2, in essence, hiding it from the fluorescence measurements.

One approach to investigating this possibility is to incorporate the measured descriptions of Ca^{2+} handling into a model that takes into consideration spatial variations of $[Ca^{2+}]_i$ within the cytoplasm. To do this, the model cell was divided into 49 concentric shells, with a small central sphere. The same equations were used to describe Ca^{2+} movements across the plasma membrane as before, and the movements of Ca^{2+} and buffers between shells were described by a diffusion equation assuming fast buffering (Eq. A27). Finally, we assumed that mitochondria are distributed uniformly throughout the cell interior and express J_{uni} with the same $[Ca^{2+}]_i$ dependence as that determined during the recovery, when $[Ca^{2+}]_i$ is expected to be more nearly uniform (see below). In this diffusion model, there are three additional parameters beyond those used in the uniform model: the diffusion coefficients of Ca^{2+} (D_{Ca}) and of the endogenous and exogenous Ca^{2+} buffers (D_{Endog} and D_{fura2}).

Fig. 5 illustrates the main findings from the diffusion model. Fig. 5 A shows the measured current and panel B illustrates the measured $[Ca^{2+}]_i$ response along with the following simulated quantities: $[Ca^{2+}]_i$ in the central and outermost shells, the spatial average of $[Ca^{2+}]_i$ calculated according to Eq. A32, and finally the spatial average calculated based on the fura-2 calibration parameters used in the original experiments (Eqs. A31 and A33). The calculations shown in Fig. 5 B were made with $D_{Endog} = 15\ \mu m^2/s$. Smaller and larger values systematically under- and overestimate the measured spatial average of $[Ca^{2+}]_i$ during depolarization, respectively (Fig. 5, C and D). Indeed, there is a distinct minimum in the error of the calculated $[Ca^{2+}]_i$ responses near this value of D_{Endog} (Fig. 5, D and E). In three cells, the optimal value of D_{Endog} fell within the range 3–15 $\mu m^2/s$, consistent with an endogenous buffer having low mobility.

We also tested how the agreement between simulated and measured responses depends jointly on D_{Endog} and D_{Fura} by varying each in the range 0–50 $\mu m^2/s$, while holding D_{Ca} constant at 300 $\mu m^2/s$. We found that the optimal combination was $D_{Endog}=15$ and $D_{Fura}=50\ \mu m^2/s$. When D_{Endog} was held at 15 $\mu m^2/s$ and D_{Fura} was varied from 0 to 50 $\mu m^2/s$, spanning the range of values used in several previous studies (see McHugh and Kenyon, 2004), the error declined slowly and monotonically as D_{Fura} approached 50 $\mu m^2/s$. Thus, over the range of expected values for D_{Fura}, the optimal value is 50 $\mu m^2/s$. Changing D_{Ca} over the range 50–300 $\mu m^2/s$, while holding $D_{Endog} = 15$ and $D_{Fura} = 50$, had relatively little effect, with sizable effects on the error being evident only when $D_{Ca} < 50\ \mu m^2/s$.

It should be noted that in Case 3 the radial nonuniformity of $[Ca^{2+}]_i$ that is observed during depolarization collapses shortly after repolarization (Fig. 5 B). Thus, analysis of (spatially averaged) $[Ca^{2+}]_i$ during the recovery is expected to provide information about the $[Ca^{2+}]_i$ dependence of Ca^{2+} buffering and transport rates that extends to Ca^{2+} handling during the onset.

In contrast to simulated responses to strong depolarization, responses to weak depolarization (Fig. 5, right) show little spatial heterogeneity during the stimulus and are not very sensitive to D_{Endog} over the range 0–25 $\mu m^2/s$ (Fig. 5, G–J). In fact, responses to weak depolarization based on the diffusion model are very similar to those deduced from the spatially uniform model. Thus, when Ca^{2+} entry rates are low, free diffusion is adequate to ensure that $[Ca^{2+}]_i$ is essentially uniform.

While these results suggest that steep $[Ca^{2+}]_i$ gradients coupled with nonlinear Ca^{2+} uptake by mitochondria may contribute significantly to the difference between measured and calculated $[Ca^{2+}]_i$ during strong depolarization, another possible contribution arises from $[Ca^{2+}]_i$ estimations based on spatially averaged fluorescence measurements (McHugh and Kenyon, 2004). In brief, the equation used to calculate $[Ca^{2+}]_i$ from fluorescence measurements depends nonlinearly on fluorescence intensity (see Eqs. A31 and A33). As a result, averaging contributions to fluorescence intensity from regions with different $[Ca^{2+}]_i$ levels can systematically underestimate the true spatial average. To examine possible contributions from this effect, we calculated the ratio of the spatially averaged fluorescence intensities at two excitation wavelengths (350 and 380 nm) based on calibration parameters from the original experiments. We then used this ratio to estimate the average $[Ca^{2+}]_i$ that would be reported by fura-2 fluorescence measurements. The results are illustrated in Fig. 5 B by the red dashed curve, which is slightly lower than the "true" spatial average of $[Ca^{2+}]_i$ calculated according to Eq. A32 (red continuous curve). These results suggest that a combination of low mobility buffers, nonlinear Ca^{2+} uptake by near-membrane mitochondria,

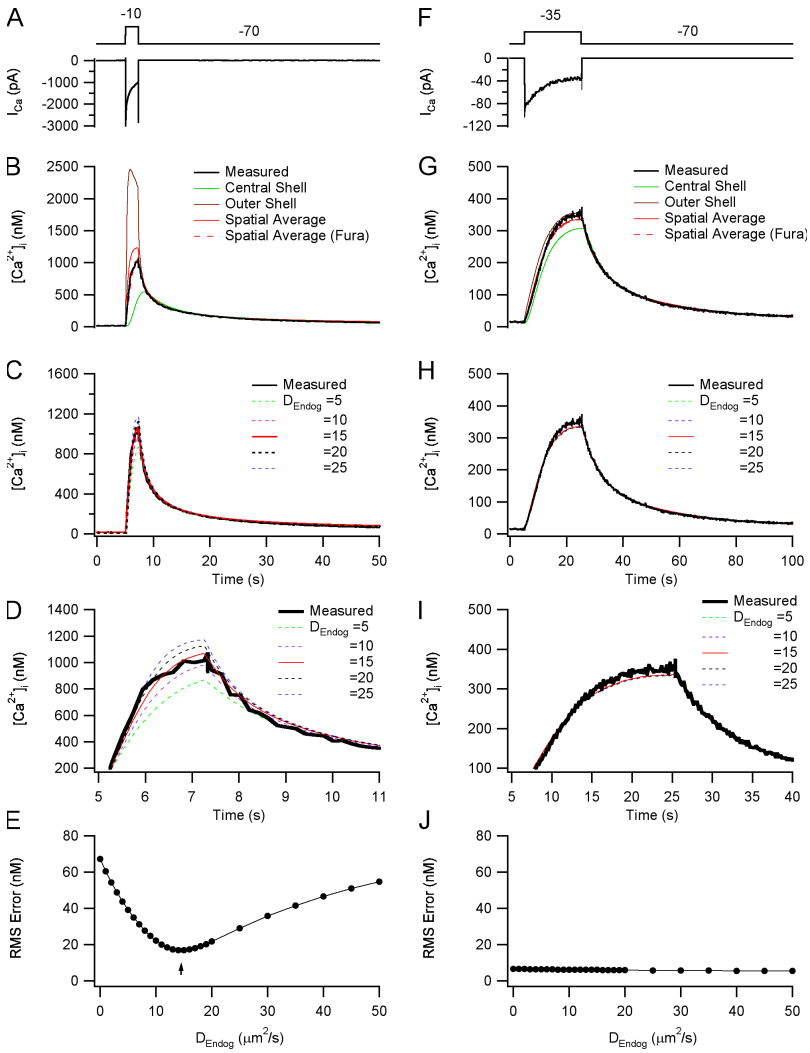

Figure 5. Analysis of $[Ca^{2+}]_i$ responses elicited by strong depolarization under conditions where mitochondrial Ca^{2+} uptake is enabled (Case 3): spatially nonuniform model. (A–E, left) Analysis of responses to strong depolarization. (F–J, right) Analysis of responses to weak depolarization. (A and F) Measured currents elicited by strong and weak depolarization, respectively. (B and G) Measured and simulated $[Ca^{2+}]_i$ responses in central sphere and outer shell, along with the calculated spatial average of $[Ca^{2+}]_i$, and the spatial average of $[Ca^{2+}]_i$ derived from calculated fluorescence (D_{Endog} = 15μm^2/s). (C and H) Responses calculated assuming different values of D_{Endog}. (D and I) Responses from C and H on an expanded scale. (E and J) Plot of the root mean squared (RMS) difference between the measured and calculated responses based on fluorescence for different values of D_{Endog}. Parameter values for the calculated response to strong depolarization were the same as in Fig. 4, Parameter values for the calculated response to weak depolarization were the same as in Fig. 3. D_{Ca} = 300 μm^2/s, D_{Fura} = 50 μm^2/s.

and underestimation of the spatial average of $[Ca^{2+}]_i$ resulting from spatially averaged fluorescence measurements accounts for the discrepancy between calculations based on the spatially uniform model and measured responses.

Case 4. Inclusion of the Mitochondrial Na/Ca Exchanger

In Cases 2 and 3, mitochondrial Ca^{2+} release was inhibited because the pipette solution did not contain added Na^+, a necessary substrate of the Na/Ca exchanger. In these cases, mitochondria can be viewed as Ca^{2+}-absorbing organelles, as long as the driving force for uptake is maintained. In this section, we examine the added contribution to Ca^{2+} dynamics from the Na/Ca exchanger, which was enabled by including Na^+ (6.5 mM) in the pipette solution. Under these conditions, depolarization from −70 to −10 mV leads to $[Ca^{2+}]_i$ currents and $[Ca^{2+}]_i$ elevations (Fig. 6, A and B) like those seen in the preceding section. However, recoveries display a slow plateau phase lasting many seconds, which is prolonged by Ca^{2+} release from mitochondria that are loaded during depolarization (Thayer and Miller, 1990; Friel and Tsien, 1994).

Measurement and Characterization of the Ca^{2+} Flux Generated by the Na/Ca Exchanger. To investigate Ca^{2+} release via the Na/Ca exchanger, we depolarized Tg-treated cells in the presence and absence of CGP 37157 (CGP), a specific inhibitor of the exchanger (Cox and Matlib, 1993; Colegrove et al., 2000a). J_{NaCa} was then measured as the CGP-sensitive component of the total cytoplasmic Ca^{2+} flux (Eq. M12, Fig. 6 C). This flux component represents Ca^{2+} release during most of the recovery (after vertical dotted line in Fig. 6 B; see shaded region in C). Flux measurements over this period are shown on an expanded scale in Fig. 6 D. We focused on the CGP-sensitive flux during this phase of the recovery, instead of during the initial rapid phase, when it is difficult to measure reliably. This has little consequence, since the CGP-sensitive flux constitutes a small fraction of the total flux during the initial phase of recovery, when $[Ca^{2+}]_i$ is high and the uniporter dominates Ca^{2+} removal.

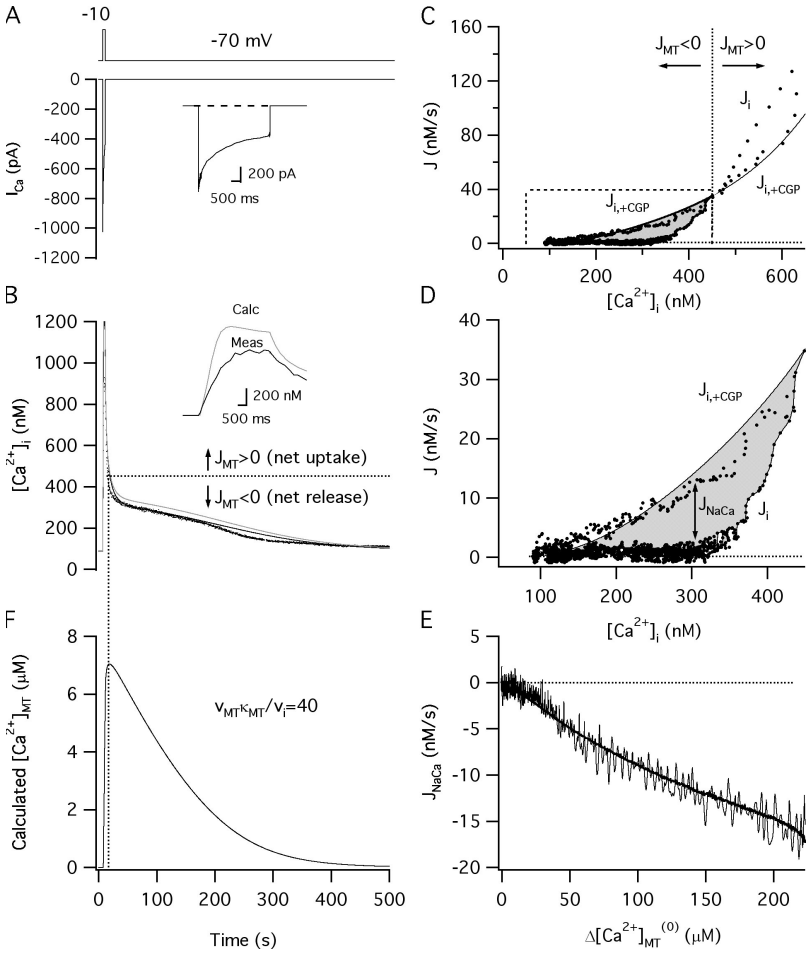

Figure 6. Analysis of the impact of the mitochondrial Na/Ca exchanger: spatially uniform model (Case 4). (A) I_{Ca} elicited by a step depolarization from −70 to −10 mV. Inset shows current on an expanded time scale. (B) $[Ca^{2+}]_i$ response elicited by this stimulus. Traces show measured $[Ca^{2+}]_i$ (dots), initial calculated response (gray trace) based on analysis of transport in the same cell using average buffering parameters from cells described in Cases 1–3. Dark trace is calculated after small changes in the parameters of $f_i\kappa_i$. Inset compares measured and calculated $[Ca^{2+}]_i$ during the period of depolarization on expanded time scale. (C) Measured fluxes during the recovery after depolarization in the absence (J_i) and presence ($J_{i,+CGP}$) of CGP-37157. Shaded region represents J_{NaCa}. Vertical dotted line marks sink-to-source transition for mitochondria in this response. Measurements over the $[Ca^{2+}]_i$ range indicated by dashed box are shown on expanded scale in D. (E) Plot of J_{NaCa} vs. $\Delta[Ca^{2+}]_{MT}^{(0)}$ during the recovery along with fitted curve from which J_{NaCa} parameters were obtained according to Eq. A22. (F) Time course of $[Ca^{2+}]_{MT}$ calculated assuming that mitochondrial volume fraction (v_{MT}/v_{Cell}) is 0.01 and buffering strength (κ_{MT}) is 4,000. Parameter values: $V_{max,Extru}$ = 29.8 nM/s, $K_{d,Extru}$ = 350 nM, n_{Extru} = 3, $f_i\kappa_{Endog}$ = 75, $f_iB_{total,Fura}$ = 75 μM, $k_{leak} = 2.6 \times 10^{-7}$ s^{-1}, $A = 1.7 \times 10^{-10}$, n_{uni} = 3.1, $\tilde{V}_{max,NaCa}$ = 3.5 μM/s, $EC_{50,NaCa}$ = 5.3 μM.

In contrast, this flux component represents a substantial fraction of J_i during the late, slow, phase of recovery and therefore strongly influences recovery kinetics (Colegrove et al., 2000b).

Analysis of J_{NaCa} is more complicated than any of the other fluxes described above because it depends on intramitochondrial free Ca^{2+} concentration ($[Ca^{2+}]_{MT}$), which was not directly measured in these experiments. In the cases analyzed above, each Ca^{2+} flux (except for J_{VSCC}) could be described as a function of measured $[Ca^{2+}]_i$. To overcome this difficulty, we used an indirect measure of $[Ca^{2+}]_{MT}$ that was derived from measurements of $[Ca^{2+}]_i$. This method makes use of the integrated mitochondrial Ca^{2+} flux during the recovery as a way to describe changes in intramitochondrial Ca^{2+} concentration during the recovery, viewed from the vantage point of the cytoplasm. This quantity is represented by $\Delta[Ca^{2+}]_{MT}^{(0)}$ (Eqs. A17 and A18). J_{NaCa} was calculated as the difference between J_i and $J_{i,+CGP}$ (shaded region in Fig. 6 D), plotted vs. $\Delta[Ca^{2+}]_{MT}^{(0)}$ (Fig. 6 E), and then fit with a saturable function of $[Ca^{2+}]_{MT}$ expressed in terms of $\Delta[Ca^{2+}]_{MT}^{(0)}$ (Eq. A22; see smooth curve), which provided estimates of the parameters of J_{NaCa}.

Reconstruction of the $[Ca^{2+}]_i$ Response. We then asked if this description of J_{NaCa}, together with the other Ca^{2+} handling systems discussed in connection with Cases 2 and 3 makes it possible to reproduce measured $[Ca^{2+}]_i$ responses. The response calculated based on measurements of Ca^{2+} removal and release rates in the same cell, and buffering parameters from Cases 1–3 above, is shown by the gray curve in Fig. 6 B. This response has the same shape as the measured response during the recovery, but slightly overestimates $[Ca^{2+}]_i$. However, small changes in the buffering parameters (<20%) led to better agreement with the measured response (Fig. 6 B, dark curve). Similar results were obtained in another cell stimulated and analyzed using the same protocol.

Fig. 6 F shows the calculated time course of $[Ca^{2+}]_{MT}$ during the response. Note that $[Ca^{2+}]_{MT}$ (t) is related to the measured quantity $\Delta[Ca^{2+}]_{MT}^{(0)}$(t) but also depends on the mitochondrial volume fraction and buffering strength (Eq. A18). This is simply because a given net Ca^{2+} flux delivered to a small mitochondrial compartment would produce a larger change in total mitochondrial Ca concentration than if the same flux were deposited into a larger volume. In addition, the impact of this change in $[Ca]_{MT}$ on intraluminal free Ca^{2+} levels

depends on the strength of intramitochondrial Ca^{2+} buffering. The calculation illustrated in Fig. 6 F assumes a mitochondrial volume fraction of 0.01 and buffering strength of 4,000, according to which $[Ca^{2+}]_{MT}$ reaches a peak of ~7 μM during depolarization. Larger or smaller values of volume fraction or buffering strength would give proportionally different values.

The simulation illustrated in Fig. 6 B is based on the spatially uniform model and overshoots measured $[Ca^{2+}]_i$ during the period of depolarization as in Case 3. Fig. 7 shows simulations that make use of the same descriptions of Ca^{2+} transport and buffering but in the context of the diffusion model. Fig. 7 B compares the calculated spatial average of $[Ca^{2+}]_i$ that would be expected from fluorescence measurements and the measured values, which are in reasonably good agreement if D_{Endog} ~5 $\mu m^2/s$.

A noteworthy feature of diffusion simulations that include mitochondrial Ca^{2+} uptake is the relatively long-lasting spatial nonuniformity of $[Ca^{2+}]_{MT}$ during the recovery (Fig. 7 C), which contrasts with the virtually complete dissipation of $[Ca^{2+}]_i$ gradients after repolarization (Fig. 7 B). The mitochondrial Ca^{2+} gradients are sustained longer than the cytoplasmic gradients because Ca^{2+} does not diffuse between mitochondria, and because the rate of release is slow compared with cytoplasmic diffusion.

Case 5. Effects of ER Ca^{2+} Uptake and Release

Fig. 8 illustrates a diffusion simulation using the same stimulus and parameter values as in Case 4, but with the addition of a second internal compartment representing the ER. We used descriptions of ER Ca^{2+} uptake and release from our previous work (Albrecht et al., 2002; Eqs. A24–26) that are based on measurements from multiple cells, since we have not obtained a complete set of flux measurements describing mitochondrial and ER Ca^{2+} transport in the same cell.

There are several interesting properties of these $[Ca^{2+}]$ responses. Inclusion of the ER does not strongly influence either cytoplasmic or mitochondrial $[Ca^{2+}]$ dynamics, consistent with the idea that under these conditions, mitochondria are more influential than the ER. The ER acts as a Ca^{2+} source during the early phase of the response, when $[Ca^{2+}]_i$ is highest, and as a sink during most of the recovery. This is consistent with the biphasic $[Ca^{2+}]_i$ dependence of the direction of net ER Ca^{2+} transport described previously in these cells (Albrecht et al., 2002). The initial decline in $[Ca^{2+}]_{ER}$ is more pronounced in the outer shells, where $[Ca^{2+}]_i$ is highest, compared with the central shells. However, in contrast to $[Ca^{2+}]_{MT}$, ER Ca^{2+} levels are spatially much more uniform than $[Ca^{2+}]_{MT}$, showing only ~5% difference between central and peripheral regions. $[Ca^{2+}]_{ER}$ displays a prolonged overshoot during the recovery that continues even after mitochondrial $[Ca^{2+}]_{MT}$ is close to its prestimulation level. This agrees with measurements of total ER Ca concentration during the recovery after depolarization in the same cells (Hongpaisan et al., 2001) as well as in neurons in cultured hippocampal slices after field stimulation (Pozzo-Miller et al., 1997). Simulations over longer times demonstrate that this overshoot is transient (unpublished data).

Comparison between Simulated and Measured Changes in Total Mitochondrial and ER Ca Concentrations. Our previous work has described depolarization-induced changes in total mitochondrial and ER Ca concentration in sympathetic neurons (Pivovarova et al., 1999; Hongpaisan et al., 2001). We found that Ca^{2+} entry leads to a time-dependent increase in $[Ca]_{MT}$ and a biphasic change in $[Ca]_{ER}$, where these measurements represent total organelle Ca concentration averaged over the entire cell. In addition, we described the spatial profile of total Ca concentration in these organelles at fixed time points during depolarization (Hongpaisan et al., 2001). It was found that mitochondria near the plasma membrane accumulate Ca at a higher rate than those situated further away. ER Ca transport is also more pronounced near the plasma membrane, but transport by this organelle favors net Ca^{2+} release. The distinct spatial variations in total organellar Ca concentration described in those studies presumably represents the combined effects of spatial variations in $[Ca^{2+}]_i$ during stimulation and intrinsic differences in Ca^{2+} handling by mitochondria and the ER. Overall, these measurements provide another opportunity to evaluate our model by comparing measured and calculated total mitochondrial and ER Ca concentration. Before presenting the results, it is important to describe how changes in intraluminal Ca concentration are calculated in the model and how these calculations can be related to measured quantities.

Calculating Changes in Intraluminal Total Ca Concentration. Intraluminal total Ca concentration ([Ca]) changes at a rate that depends on the rate of net Ca^{2+} transport between organelle and cytoplasm, as well as organelle volume. However, all transport rates were measured based on changes in cytoplasmic Ca^{2+} concentration. For example, we measured the mitochondrial free Ca^{2+} flux (J_{MT}) as the FCCP-sensitive component of the cytoplasmic Ca^{2+} flux. This flux can be interpreted as the net Ca^{2+} flux between mitochondria and the cytoplasm ($\tilde{J}_{MT}$) divided by the product of the cytoplasmic volume v_i and k_i (Eq. M6):

$$J_{MT} = \frac{\tilde{J}_{MT}}{v_i \kappa_i}$$

To calculate changes in $[Ca]_{MT}$ during stimulation, a different quantity is needed, $\tilde{J}_{MT} / v_{MT}$, which can be

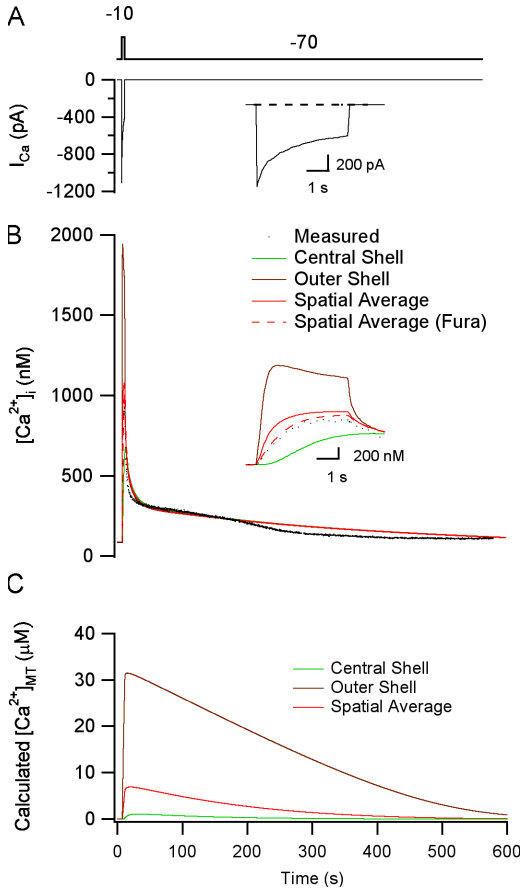

Figure 7. Analysis of the impact of the mitochondrial Na/Ca exchanger (Case 4): spatially nonuniform model. Parameters for plasma membrane and uniporter transport are the same as in Fig. 6. (A) I_{Ca}. (B) Measured and calculated $[Ca^{2+}]_i$ responses. (C) Calculated $[Ca^{2+}]_{MT}$ responses. Insets in A and B show current and $[Ca^{2+}]_i$ traces on an expanded scale. See insets for trace identification (same as Fig. 5). Diffusion coefficients (in $\mu m^2/s$): $D_{Ca} = 300$, $D_{Fura} = 50$, $D_{Endog} = 5$.

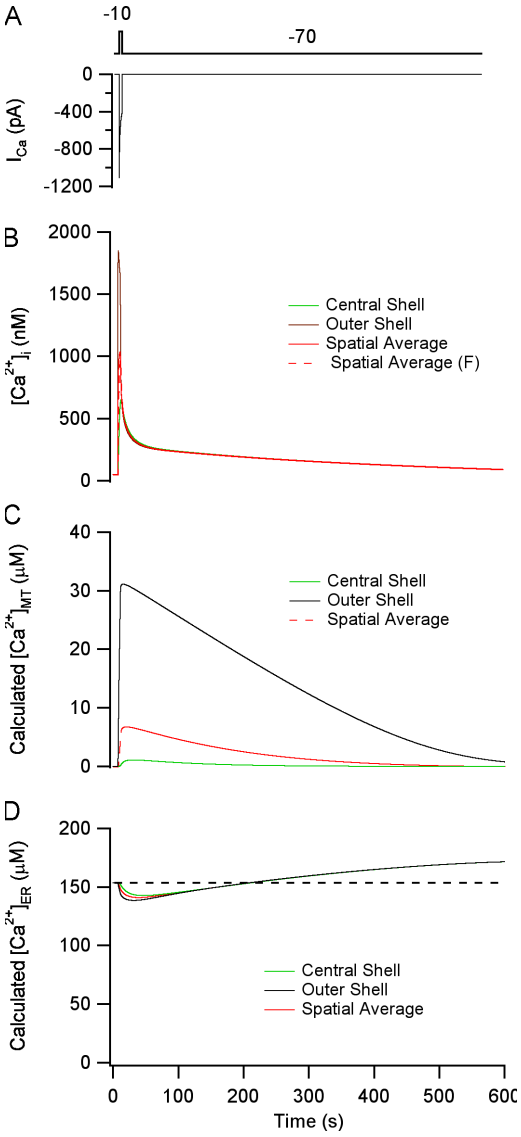

Figure 8. Effect of including ER Ca^{2+} uptake (Case 5). Calculations based on the same model used in Fig. 7 but with the addition of a second compartment representing the ER. ER Ca^{2+} uptake and release are described in Eqs. A24–A26. (A) I_{Ca}. (B) Calculated $[Ca^{2+}]_i$ responses. (C) Calculated $[Ca^{2+}]_{MT}$ responses. (D) Calculated $[Ca^{2+}]_{ER}$ responses. See insets for identification of traces. Parameter values for plasma membrane and mitochondria are the same as in Fig. 7. ER parameters: $v_{ER}/v_i = 0.05$, $\kappa_{ER} = 20$, $V_{max,SERCA} = 2146 \times 10^{-9}$ nM/s, $EC_{50,SERCA} = 30 \times 10^{-9}$ nM, $n_{SERCA} = 2.5$, $P_{basal} = 0.01\ s^{-1}$, $P_{max,RyR} = 0.05\ s^{-1}$, $EC_{50,RyR} = 2{,}600$ nM, nRyR = 1.

integrated between any two times to give the change in $[Ca]_{MT}$ between those times. However, given an estimate of v_{MT}/v_{Cell}, $\tilde{J}_{MT}/v_{MT}$ can be determined from the measured quantities J_{MT} and $f_i\kappa_i$ as follows:

$$\frac{\tilde{J}_{MT}}{v_{MT}} = J_{MT}\left[\kappa_i\left(\frac{v_i}{v_{MT}}\right)\right] = J_{MT}\left[f_i\kappa_i\left(\frac{v_{Cell}}{v_{MT}}\right)\right]. \quad (6)$$

An analogous approach can be used to estimate the fluxes that lead to changes in total ER Ca concentration. These considerations underscore the importance of organellar volume fraction in calculating changes in total Ca concentration from measured free cytoplasmic Ca^{2+} fluxes. Volume fraction can be estimated from the fractional area occupied by the respective organelles in fixed sections (Weibel and Elias, 1967). Recent estimates in sympathetic neurons give 0.01–0.04 as the range for mitochondria (Andrews, S.B., personal communication), which is lower than the value we used previously (0.1).

Measurements of ER volume fraction are more difficult using this approach. Our previous estimate was ~0.05–0.10 (Albrecht et al., 2002). A complementary approach is to use the model to determine the ER

volume fraction for which the calculated resting $[Ca]_{ER}$ agrees with the measured value (~3.6 mM; Hongpaisan et al., 2001). Using $\kappa_{ER} = 20$ (Mogami et al., 1999), this approach yielded a value of 0.043. Such a method for estimating mitochondrial volume fraction is not possible because resting $[Ca]_{MT}$ is difficult to measure (Pivovarova et al., 1999).

With estimates of mitochondrial and ER volume fractions in hand, we asked if calculated and measured spatial averages of $[Ca]_{MT}$ and $[Ca]_{ER}$ agree at 45 s during depolarization. To make this comparison, it was necessary to construct an appropriate I_{Ca} for use in the model calculations. This is because the total Ca concentration was measured in sections from cells in ganglia that were rapidly frozen at different times during stimulation with 50 mM K^+, making simultaneous measurement of I_{Ca} impractical. However, control experiments show that under these conditions of stimulation, the membrane potential is steady at ~−20 mV (Friel and Tsien, 1992). In lieu of direct measurements of I_{Ca}, we fit a representative Ca^{2+} current elicited by depolarization to the same potential with a triexponential function plus a constant. The steady-state value of the fitted curve was constrained to give a simulated $[Ca^{2+}]_i$ level at 45 s that agrees with measured values in cells exposed to 50 mM K^+ (618 ± 86 nM, $n = 4$ cells). For these simulations, the fura-2 concentration was set to zero because cells in which elemental analysis was performed were not loaded with a Ca^{2+} indicator. This caused simulated $[Ca^{2+}]_i$ to increase more rapidly during stimulation, but as expected, the steady level approached during maintained stimulation was not altered (unpublished data).

Comparison between Measured and Calculated Spatially Averaged Total Ca Concentrations. Fig. 9 (A–D) shows the time courses of I_{Ca}, $[Ca^{2+}]_i$, $[Ca]_{MT}$, and $[Ca]_{ER}$ simulated using parameters for plasma membrane, mitochondrial, and ER Ca^{2+} transport from Case 5 above. According to the model, the spatially averaged total mitochondrial Ca concentration increases throughout the period of Ca^{2+} entry, attaining a value at 45 s (21.6 mM; Fig. 9 C, red trace) that is between the measured values determined by EDX (8.7 mM) and EELS (29.7 mM) (Hongpaisan et al., 2001), where the latter average was calculated from the spatially resolved measurements according to Eq. A32. Total ER Ca concentration declined from its resting level (3.6 mM) under the influence of graded net Ca^{2+}-induced Ca^{2+} release (CICR), reaching 3.5 and 3.0 mM at 10 and 45 s, respectively. This can be compared with EDX measurements at these times (2.9 and 3.2 mM; Hongpaisan et al., 2001). As expected, the calculated changes in $[Ca]_{MT}$ and $[Ca]_{ER}$ are inversely proportional to the respective volume fractions. Fig. 9 E (left) shows how for mitochondria the absolute difference between the measured (EELS) and calculated spatial average of $[Ca]_{MT}$ at 45 s depends on volume fraction. There is a distinct minimum at a volume fraction of 0.0065, where the calculated and measured values are nearly equal.

Comparison between Measured and Calculated Spatially Resolved Total Ca Concentrations. Finally, we examined the spatial profiles of $[Ca^{2+}]_i$, $[Ca]_{MT}$, and $[Ca]_{ER}$ at different times during depolarization (Fig. 9, F–H). As in previous studies (Neher and Augustine, 1992; Hua et al., 1993), the spatial profile of $[Ca^{2+}]_i$ shows steep gradients during the first few seconds of depolarization that dissipate with time (Fig. 9 F). Over the same period, peripheral $[Ca]_{MT}$ increases more rapidly than in more central regions (Fig. 9 G) because $[Ca^{2+}]_i$ is higher near the plasma membrane and because the rate of Ca^{2+} uptake by the uniporter increases steeply with $[Ca^{2+}]_i$. The measured spatial profiles of $[Ca]_{MT}$ (EELS) and $[Ca]_{ER}$ (EDX) at 45 and 10 s, respectively, are shown in Fig. 9 (G and H, symbols) (Hongpaisan et al., 2001). The calculated changes in total organelle Ca concentration were inversely proportional to volume fraction, and the steepness of the spatial profile depended strongly on D_{Endog}, with small values favoring steeper gradients of both $[Ca]_{MT}$ and $[Ca]_{ER}$. However, the spatial averages of $[Ca]_{MT}$ and $[Ca]_{ER}$ at fixed times were relatively insensitive to D_{Endog} (unpublished data). Assuming a mitochondrial volume fraction of 1%, the RMS error between the calculated and measured spatial profile of $[Ca]_{MT}$ was minimal when $D_{Endog} = 0$ (Fig. 9 E, right; see Fig. 9 G, dashed curve). We found that with mitochondrial volume fraction set to 0.65–1% and $D_{Endog} = 0$–5 $\mu m^2/s$, model calculations and experimental measurements were very similar (Fig. 9 G). Calculations of $[Ca]_{ER}$ were in good agreement with measurement in all regions except the outer shell, where the measurements suggest more pronounced Ca release from the ER during the first 10 s of stimulation. Overall, these results indicate that the diffusion model provides a good quantitative description of Ca^{2+} handling by mitochondria and the ER in sympathetic neurons, except that it appears to underestimate the magnitude of evoked changes in ER total Ca concentration within 2–4 μm of the plasma membrane.

DISCUSSION

This work describes the reconstruction of depolarization-evoked Ca^{2+} responses based on measured characterizations of surface membrane, mitochondrial, and ER Ca^{2+} transport and cytoplasmic Ca^{2+} buffering in the same cell type. When incorporated into a diffusion model with compartments representing the cytoplasm, mitochondria, and ER, these characterizations make it possible to account quantitatively for many features of depolarization-induced Ca^{2+} responses. These include the time course of spatially averaged cytoplasmic Ca^{2+} concentration during and after depolarization, the

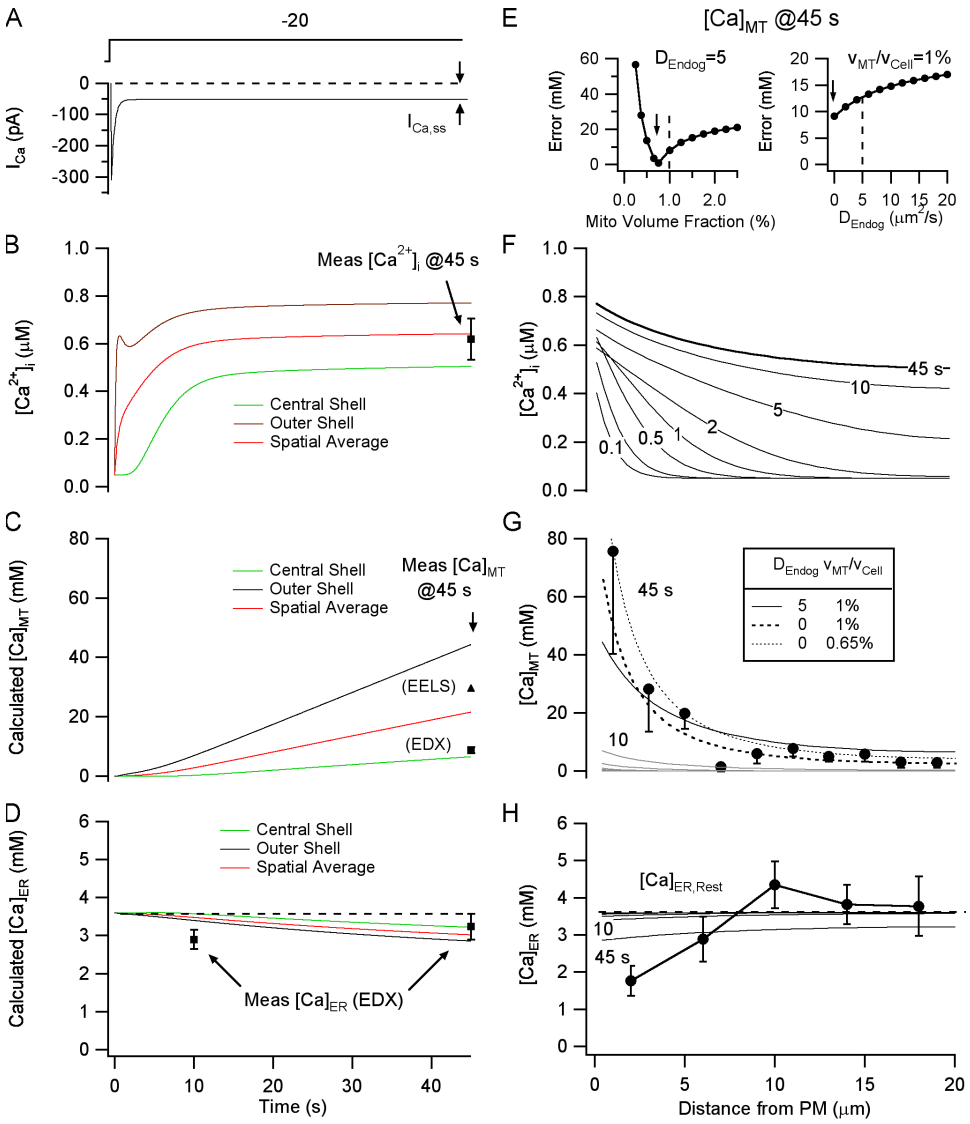

Figure 9. Comparison between calculated and measured changes in total mitochondrial and ER Ca concentrations induced by a 45-s depolarization. (A) I_{Ca} waveform representing Ca^{2+} entry during a steady depolarization to −20 mV based on triexponential fit to measured current elicited by a 5.3-s depolarization to the same voltage, extrapolated to a steady-state value that produces a steady $[Ca^{2+}]_i$ elevation similar to the mean level observed after 45 s depolarization with 50 mM K^+. (B) $[Ca^{2+}]_i$. (C) $[Ca]_{MT}$. (D) $[Ca]_{ER}$. Symbols in B–D indicate measurements for comparison with calculated spatial average of $[Ca^{2+}]_i$, $[Ca]_{MT}$, and $[Ca]_{ER}$ (see arrows). (E, left) Absolute difference between calculated and measured spatial average of $[Ca]_{MT}$ at 45 s as a function of mitochondrial volume fraction (v_{MT}/v_{Cell}) calculated with D_{Endog} = 5. A distinct minimum occurs at 0.65% (arrow). (E, right) RMS error in calculated spatial profile of $[Ca]_{MT}$ at 45 s as a function of D_{Endog} calculated with v_{MT}/v_{Cell} = 0.01. The error is minimal when D_{Endog} = 0 (arrow). (F) Calculated spatial profiles of $[Ca^{2+}]_i$ at indicated times during depolarization. (G) Calculated spatial profiles of $[Ca]_{MT}$ at indicated times during depolarization (continuous traces) with v_{MT}/v_{Cell} = 0.01 and D_{Endog} = 5 along with EELS measurement at 45 s (symbols). Interrupted traces show calculated profiles at 45 s for different values of v_{MT}/v_{Cell} and D_{Endog} (see table, inset). (H) Calculated spatial profiles of $[Ca^{2+}]_{ER}$ at indicated times during depolarization (continuous traces) along with EDX measurement of $[Ca]_{ER}$ at 10 s (symbols). Unless otherwise stated, parameters are the same as in Fig. 8.

spatial averages of intraluminal mitochondrial and ER total Ca concentration at a fixed time (45 s) after depolarization, and the spatial profile of $[Ca]_{MT}$ at the same time point. Overall, these results indicate that the main Ca^{2+} handling systems operating in these neurons have been taken into consideration, and that they have been described with sufficient accuracy to account for the measurements. Our model can be used to study responses to other stimuli in the same cells, and a similar approach could be used to investigate Ca^{2+} dynamics in other cells, once the specific Ca^{2+} handling systems expressed in these cells are described.

Approximations Used in the Model

We started with a model in which cytoplasmic Ca^{2+} was assumed to be uniformly distributed, and found that this model could account for responses elicited by weak but not strong depolarization. However, responses to strong depolarization could be accounted for if the Ca^{2+} handling descriptions were included in a diffusion model that takes into consideration radial variations in $[Ca^{2+}]_i$. The two models agree in the case of weak depolarization, as expected if the uniform model describes a limiting case of the more general diffusion model when radial $[Ca^{2+}]_i$ gradients are shallow.

Our model cell was assumed to be spherically symmetrical with a radially uniform distribution of organelles. The finding that model calculations were close to measured responses indicates that deviations from spherical symmetry and radially uniform organelle distribution are not critical for the spatiotemporal properties of the measured $[Ca^{2+}]_i$, $[Ca]_{ER}$, and $[Ca]_{MT}$

signals. Nevertheless, there was a hint that our description of Ca^{2+} handling near the plasma membrane was not sufficiently detailed. While the model reproduced the decline in $[Ca]_{ER}$ observed near the plasma membrane, it underestimated the magnitude of this decline measured at 10 s. This points to a need to consider additional Ca^{2+} regulatory processes in this subcellular region (see below).

Another simplifying assumption made in constructing the model is that within both the mitochondria and the ER, free intraluminal Ca concentration is proportional to total Ca concentration. Evaluation of this assumption was not possible because, although we made use of previous measurements of total organelle Ca concentration (free + bound), we did not measure intraluminal free Ca^{2+} concentration. There is evidence that Ca^{2+} buffering inside mitochondria is complex (David et al., 2003; Nicholls and Chalmers, 2004). By regulating intraluminal free Ca^{2+} levels, this system could influence the rate of mitochondrial Ca^{2+} release, thereby contributing to the level and duration of the slow $[Ca^{2+}]_i$ recovery that follows strong stimulation. This, in turn, would be expected to affect all processes that are sensitive to $[Ca^{2+}]_i$.

As a stimulus, we used Ca^{2+} currents elicited by step depolarizations from a hyperpolarizing membrane potential. While not a naturally occurring physiological stimulus, this does provide a convenient way to perturb Ca^{2+} regulation so that contributions from different regulatory systems can be investigated. Other, more physiological, model inputs are possible, including measured action potential waveform-induced Ca^{2+} currents, whose effects could then be compared with measured $[Ca^{2+}]_i$ responses.

Stimulus-induced Changes in Mitochondrial and ER Total Ca Concentrations

Our previous results showed that Ca^{2+} entry induced by strong depolarization stimulates mitochondrial Ca^{2+} accumulation and net ER Ca^{2+} release. Both of these observations were reproduced by the model. Difference in the direction of net Ca transport by these organelles can be explained by differences in the intrinsic $[Ca^{2+}]_i$ sensitivity of the pathways by which they take up and release Ca^{2+} (Friel, 2003). High $[Ca^{2+}]_i$ levels generated near sites of Ca^{2+} entry during stimulation drive powerful Ca^{2+} accumulation by peripheral mitochondria because at these concentrations, Ca^{2+} uptake via the uniporter is much faster than Ca^{2+} release via the Na/Ca exchanger. Net Ca^{2+} release by the ER occurs because at these same $[Ca^{2+}]_i$ levels the rate of passive Ca^{2+} release exceeds the rate of uptake by SERCAs. At high $[Ca^{2+}]_i$ during strong depolarization, net Ca^{2+} transport by mitochondria dominates, accounting for the major role it plays in shaping $[Ca^{2+}]_i$ responses under these conditions (Herrington et al., 1996). On the other hand, at the lower $[Ca^{2+}]_i$ levels reached during weak depolarization, the ER accumulates Ca^{2+} and is more influential than mitochondria (Albrecht et al., 2002).

To compare calculated changes in mitochondrial and ER total Ca concentrations with measured values, we used Ca^{2+} transport descriptions obtained from cytoplasmic Ca^{2+} measurements. To calculate intraluminal total Ca concentration, it was necessary to specify the mitochondrial and ER volume fractions. Information about these parameters is incomplete, which introduces uncertainty into calculated intraluminal total Ca concentrations. However, it is possible to estimate ranges for these parameters. One approach is to measure the fraction of the cellular area occupied by the respective organelles in tissue sections (Weibel and Elias, 1967). For mitochondria this gives ~1–4%. For the ER, expected values are in the range 4–5%. We found that for volume fractions within these ranges, the calculated values of total mitochondrial and ER Ca concentration during depolarization closely resemble the measured ones; smaller or larger volume fractions give proportionately different calculated values. For mitochondria, the measured spatial average of $[Ca]_{MT}$ at 45 s during a 50 mM K^+ depolarization (29.7 mM, based on EELS measurements) matched the calculated value when volume fraction is 0.65%, slightly below the estimated range (1–4%). For the ER, a value of 4.3% gave an identity between the measured and calculated resting $[Ca]_{ER}$. It should be noted that because mitochondrial volume fraction estimates are based on measurements of the area enclosed by mitochondria in tissue sections, they include regions outside the mitochondrial matrix and therefore tend to overestimate the desired quantity. This may help explain why the optimal value (0.65%) was <1%.

We found that the model could account for elevations in $[Ca^{2+}]_i$ during strong depolarization, as long as endogenous cytoplasmic buffers are assumed to have low mobility (D_{Endog} ~5–15 $\mu m^2/s$). This also led to agreement between the calculated and measured spatial profile of $[Ca]_{MT}$ at a fixed time during stimulation, although in this case simulations agreed more closely with measurements when D_{Endog} ~0–5 $\mu m^2/s$. In contrast to the high sensitivity of the spatial profile of $[Ca]_{MT}$ to D_{Endog} over the range 0–15 $\mu m^2/s$, there was a comparatively low sensitivity to changes in the diffusion coefficients of fura-2 (D_{Fura}) and Ca^{2+} (D_{Ca}) within the ranges 20–50 and 100–300 $\mu m^2/s$.

Comparison between Measured and Calculated Near-Membrane Total Organelle Ca Concentrations

In addition to providing a framework for testing hypotheses regarding basic mechanisms, Ca^{2+} regulatory models can also help point out inadequacies in our understanding. There was a discrepancy between calculated and measured total ER Ca concentration in

the outer 2–4-μm shell, where $[Ca^{2+}]_i$ is expected to undergo the highest, and fastest, elevations in responses to Ca^{2+} entry. There was also a hint that the calculated value of $[Ca]_{MT}$ underestimates the measured value in this region, unless it is assumed that $D_{Endog} \sim 0$, which falls outside the range of values (5–15 $\mu m^2/s$) that were optimal for reconstructing $[Ca^{2+}]_i$ responses to strong depolarization. The basis for these discrepancies is not clear, but it is possible that they reflect inaccuracies or omissions in the description of Ca^{2+} handling in sympathetic neurons. For example, previous work has described a rapid mode of mitochondrial Ca^{2+} uptake (RaM; Buntinas et al., 2001) that was not explicitly included in the model. Such a mechanism would be expected to enhance Ca^{2+} loading by peripheral mitochondria, although it would also diminish the rate of ER Ca^{2+} release by reducing $[Ca^{2+}]_i$ elevations in the same region. It is also possible that the spatial distribution of Ca^{2+} handling systems was not accurately represented in the model. For example, previous reports have suggested that the distribution of ryanodine receptors falls off with distance from the plasma membrane (Akita and Kuba, 2000; McDonough et al., 2000). A higher density of Ca^{2+} release sites near sites of Ca^{2+} entry could promote local regenerative Ca^{2+} release that amplifies near-membrane $[Ca^{2+}]_i$ elevations, which would secondarily enhance Ca^{2+} loading by peripheral mitochondria. Including more realistic descriptions of the spatial distribution of organelles is an important area for model refinement (Means et al., 2006). However, it should be noted that, despite the assumption that organelles are distributed uniformly, the differences between measured and calculated values of $[Ca]_{MT}$ and $[Ca]_{ER}$ were in most cases within the level of uncertainty in the measurements. This supports the conclusion that the major features of Ca regulation have been included. Measurements of Ca^{2+} levels at higher spatial and temporal resolution will provide the basis for developing and evaluating more refined models of these and other cells, and accounting for such measurements will require consideration of more detailed features of cell structure and transporter distribution.

Characterization of Ca^{2+} Fluxes in Intact Cells

A novel feature of this study is that it provides enough information about Ca^{2+} handling in a particular cell type to permit quantitative comparisons between measured and calculated Ca^{2+} responses. This required the following: (a) a "complete" set of flux descriptions, such that the sum of the individual flux components equals the total flux driving changes in Ca^{2+} concentration; (b) measurement and characterization of the individual fluxes. We did this by suppressing transport by one or more pathway(s) using specific inhibitors and measuring the drug-sensitive and -resistant components of the total flux. It was also necessary to (c) identify the "independent" variables that control the activity of the transport systems responsible for the measured fluxes. While multiple variables influence Ca^{2+} transport (e.g., temperature, pH, ATP levels, and $[Ca^{2+}]$) only some of these change appreciably during an evoked Ca^{2+} response. This distinguishes between quantities whose variation contributes to changes in transport rate during responses, from those that are approximately constant and can be regarded as parameters. Another requirement was (d) a description of the functional dependence of transport rate on the independent variables. Ideally, this step would use analytical expressions derived from mechanistic considerations, but empirical descriptions are also valid as long as they adequately describe the relationship between the fluxes and the independent variables. In the case of J_{uni}, we started with a sigmoidal function of $[Ca^{2+}]_i$ that is expected to be centered around ~10–20 μM (for review see Gunter and Gunter, 1994). Since unique parameter values cannot be obtained for this equation when $[Ca^{2+}]_i$ is well below the midpoint for activation (<1 μM), we switched to a power function approximation that is valid at low $[Ca^{2+}]_i$. This provided a good description of the way J_{uni} varies with $[Ca^{2+}]_i$ but gave different parameter values when fit over low and high ranges of $[Ca^{2+}]_i$, suggesting a more complex $[Ca^{2+}]_i$ dependence of the uniporter, or functionally dependent parameters (see Appendix). However, despite this, the power function description of the $[Ca^{2+}]_i$ dependence of J_{uni} was adequate to describe the contribution from the uniporter to $[Ca^{2+}]_i$ dynamics. Finally, (e) it was necessary to incorporate the rate descriptions into a model with a defined compartmental structure, geometry, and transporter distribution.

Relating measured flux components to known transport pathways was facilitated by the use of blockers under conditions that favor inhibition of a single pathway. J_{uni} was measured as the FCCP-sensitive component of the total cytoplasmic Ca^{2+} flux in cells where Ca^{2+} release was inhibited using Na^+-free pipette solutions. In this case, the FCCP-resistant flux provided a description of Ca^{2+} extrusion (J_{Extru}). To enable Ca^{2+} release via the Na/Ca exchanger (Case 4), Na^+-containing pipette solutions were used. In this case, $J_{Na/Ca}$ was taken as the CGP-sensitive component of the total flux, and the total mitochondrial Ca^{2+} flux (J_{MT}) was measured as the FCCP-sensitive flux. Here, the CGP-resistant flux was used to describe Ca^{2+} removal ($J_{Extru} + J_{uni}$). In this case, J_{Extru} may have included an additional component representing Ca^{2+} entry via NCX, operating in reverse, that would not have been present when experiments were performed with low internal Na^+. As described in Materials and methods, this would not be expected to interfere with our measurement of $J_{Na/Ca}$ as long as NCX contributes equally to the total flux and the CGP-resistant component of this flux. Contributions from NCX in Case 4 would impart a

voltage dependence to Ca^{2+} extrusion, introducing an error in the Ca^{2+} removal rate during depolarization when calculated based on measurements during the recovery. However, simulated responses agreed with measurements during both the response onset and recovery, arguing that this source of error is small. Under physiological conditions, the presence of extracellular Na^+ would cause NCX to act as an extrusion system (Herrington et al., 1996; Suzuki et al., 2002; Wanaverbecq et al., 2003). More detailed analysis of the components of J_{Extru}, including NCX in the presence and absence of extracellular Na^+, will require future experiments.

Spatial Heterogeneity of Evoked Ca Signals

Our flux characterizations were based on analysis of spatially averaged $[Ca^{2+}]_i$ measurements during the recovery after stimulation. These characterizations, in the context of a spatially uniform model, provided a good description of measured responses to weak depolarization. This indicates that spatial nonuniformities of intracellular Ca^{2+} levels are not highly influential in shaping responses to weak depolarization. We suggest that under these conditions, Ca^{2+} entry is slow enough compared with diffusion that pronounced Ca^{2+} gradients do not develop. On the other hand, we found that strong depolarization elicits responses that are not consistent with the uniform model, but are consistent with a diffusion model that includes the same Ca^{2+} handling descriptions but considers radial variations in intracellular $[Ca^{2+}]$ levels. This suggests that with the higher Ca^{2+} entry rates observed during strong depolarization, diffusion is not fast enough to ensure near-spatial uniformity of $[Ca^{2+}]_i$. According to this model, cytoplasmic $[Ca^{2+}]$ gradients virtually collapse after Ca^{2+} entry ceases. Thus, measurements of average $[Ca^{2+}]_i$ during the recovery would be expected to provide a good estimate of local $[Ca^{2+}]_i$ near sites of extrusion and uptake, which can then be used to characterize the $[Ca^{2+}]_i$ dependence of transport via these pathways, even after strong depolarization.

The diffusion model suggests that in contrast to cytoplasmic $[Ca^{2+}]_i$, the spatial nonuniformity of mitochondrial total Ca concentration that develops during depolarization does not dissipate rapidly after repolarization, but persists for hundreds of seconds. While we do not have direct experimental verification of this at present, this would mean that during the recovery, mitochondrial Ca^{2+} release rate is spatially nonuniform. This raises two questions. First, how can radial nonuniformities of intramitochondrial Ca levels persist while $[Ca^{2+}]_i$ is nearly uniform? Second, how would persistence of $[Ca]_{MT}$ gradients impact our measurements of mitochondrial Ca^{2+} fluxes?

Mitochondrial Ca^{2+} fluxes were calculated based on measurements of spatially averaged $[Ca^{2+}]_i$ during the recovery, which according to the model, becomes nearly uniform shortly after Ca^{2+} entry ends. However, the model also predicts that mitochondrial [Ca] gradients are more persistent. This is because the only pathway for dissipating these gradients, the Na/Ca exchanger, releases Ca^{2+} slowly compared with the rate of cytoplasmic Ca^{2+} diffusion. As a result, at each point in time during the recovery, our measurement of J_{NaCa} must be interpreted as a spatial average of the release rate that can be related to (spatially averaged) $[Ca^{2+}]_i$ at that time. Our description of J_{NaCa} was adequate to describe how mitochondrial Ca^{2+} release contributed to the slow plateau phase of recovery seen in previous studies (Thayer and Miller, 1990; Colegrove et al., 2000a). Our results also suggest that spatial heterogeneity of $J_{Na/Ca}$ has less impact on the recovery of $[Ca^{2+}]_i$ than of intramitochondrial Ca levels, given the similarity of calculated recoveries using the spatially uniform and nonuniform models (compare Figs. 6 and 7). Nonetheless, the recoveries are not identical and methods for functionally characterizing J_{NaCa} with subcellular resolution would be useful.

Regarding the functional impact of spatially nonuniform Ca^{2+} loading by mitochondria, it has been shown that Ca^{2+} can positively regulate mitochondrial ATP production (Robb-Gaspers et al., 1998). One possibility is that Ca^{2+} uptake by near-membrane mitochondria leads to an increase in the local availability of ATP, helping to fuel ion transport near the surface membrane in the aftermath of stimulation and aid in restoring the resting state.

Role of CICR

Our results support a role for CICR in shaping depolarization-induced Ca^{2+} responses, although owing to the relatively slow rate of release compared with the rates of transport by mitochondria, the impact on $[Ca^{2+}]_i$ responses elicited by strong depolarization is small. This is supported by the weak effect of thapsigargin on $[Ca^{2+}]_i$ responses elicited by strong depolarization (Hongpaisan et al., 2001) and the subtle difference between simulated responses in the presence and absence of ER Ca^{2+} transport (Figs. 7 and 8). Two recent studies have suggested that $[Ca^{2+}]_i$ elevations elicited by action potential–induced Ca^{2+} entry in amphibian sympathetic neurons depends almost entirely on CICR (Akita and Kuba, 2000; Cseresnyes and Schneider, 2004). This conclusion is based on the observation that inhibiting ER Ca^{2+} transport by exposure to sarco/endoplasmic reticulum Ca^{2+} ATPase (SERCA) inhibitors reduces or eliminates AP-induced increases in $[Ca^{2+}]$. While our measurements do not address this point specifically, it is important to reconcile experimental and modeling results performed on different space and time scales. This should help answer important questions regarding the role of microheterogeneity in Ca^{2+} regulation, e.g., near plasma membrane sites of Ca^{2+} entry, and the relative role of brief/local elevations in $[Ca^{2+}]_i$ vs. more prolonged and global increases in regulating Ca^{2+}-dependent processes within the cell.

APPENDIX

Surface Membrane Ca^{2+} Transport: J_{VSCC}, J_{Extru}

When Ca^{2+} uptake and release by mitochondria and the ER are inhibited, the only remaining components of $\tilde{J}_i$ represent the net Ca^{2+} flux across the plasma membrane ($\tilde{J}_{PM}$). We distinguished two components of $\tilde{J}_{PM}$: Ca^{2+} entry through voltage-gated Ca^{2+} channels ($\tilde{J}_{VSCC}$), and Ca^{2+} extrusion ($\tilde{J}_{Extru}$), representing contributions from all other surface membrane Ca^{2+} transport pathways, including pumps and leaks. Since these pathways operate in parallel, their contributions to $\tilde{J}_i$ are additive. Therefore,

$$\frac{d[Ca^{2+}]_i}{dt} = -\frac{\tilde{J}_i}{v_{Cell}(f_i\kappa_i)} = -\frac{\tilde{J}_{VSCC} + \tilde{J}_{Extru}}{v_{Cell}(f_i\kappa_i)}. \quad \text{(A1)}$$

This equation can be recast into a form that is more easily related to measured quantities:

$$\frac{d[Ca^{2+}]_i(t)}{dt} = -\left[\frac{I_{Ca}(t)}{2Fv_{Cell}f_i\kappa_i} + J_{Extru}\right] \quad \text{(A2)}$$

using the following relations:

$$\tilde{J}_{VSCC} = \frac{I_{Ca}}{2F}, \qquad J_{Extru} = \frac{\tilde{J}_{Extru}}{v_{Cell}(f_i\kappa_i)} \quad \text{(A3)}$$

and F is the Faraday constant. We plotted J_{Extru} vs. $[Ca^{2+}]_i$ and fit with the following equation, which describes a parallel pump/leak system whose overall transport rate depends on $[Ca^{2+}]_i$:

$$J_{Extru} = J_{PMCA} + J_{leak}, \quad \text{(A4)}$$

where

$$J_{PMCA} = \frac{V_{\max,PMCA}}{\left(1+\left[\frac{K_{d,PMCA}}{[Ca^{2+}]_i}\right]^{n_{PMCA}}\right)} \quad \text{(A5)}$$

$$J_{leak} = k_{leak}\left([Ca^{2+}]_i - [Ca^{2+}]_o\right).$$

This equation incorporates the finding that in sympathetic neurons treated with FCCP and Tg, the rate of Ca^{2+} removal at each point in time during the recovery depends on the $[Ca^{2+}]_i$ level at that time. Thus, the time dependence of J_{Extru} during the recovery is derived from the time dependence of $[Ca^{2+}]_i$:

$$J_{Extru}(t) = J_{Extru}\left([Ca^{2+}]_i(t)\right). \quad \text{(A6)}$$

It should be noted that in some cells (e.g., human T cells) Ca^{2+} extrusion via the PMCA is time dependent (Bautista et al., 2002). When fitting Eqs. A4 and A5 to J_{Extru} measurements during the recovery (as in Fig. 2 C), we reduced the number of free parameters by requiring that $J_{Extru} = 0$ when $[Ca^{2+}]_i$ is at its resting level, making it possible to solve for k_{leak} in terms of the remaining parameters.

Mitochondrial Ca^{2+} Uniporter: J_{uni}

To investigate the contribution from mitochondrial Ca^{2+} uptake via the uniporter in isolation from Ca^{2+} release by the mitochondrial Na/Ca exchanger, responses were also elicited in the absence of FCCP, using either Na^+-free pipette solutions or application of CGP to inhibit mitochondrial Ca^{2+} release. In this case, $\tilde{J}_i$ includes a third component representing the uniporter:

$$\frac{d[Ca^{2+}]_i}{dt} = -\frac{\tilde{J}_{VSCC} + \tilde{J}_{Extru} + \tilde{J}_{uni}}{v_{Cell}(f_i\kappa_i)}. \quad \text{(A7)}$$

As in Case 1, this equation can be recast into a form that is more easily related to measured quantities:

$$\frac{d[Ca^{2+}]_i}{dt} = -\left[\frac{I_{Ca}}{2Fv_{Cell}(f_i\kappa_i)} + \left(J_{Extru} + J_{uni}\right)\right], \quad \text{(A8)}$$

where

$$J_{uni} = \frac{\tilde{J}_{uni}}{v_{Cell}(f_i\kappa_i)}. \quad \text{(A9)}$$

We characterized the sum ($J_{Extru} + J_{uni}$) quantitatively as described in Colegrove et al. (2000a). In brief, this flux was measured by calculating $-d[Ca^{2+}]_i/dt$ during the recovery after depolarization-induced $[Ca^{2+}]_i$ elevations in Tg-treated cells in the absence of FCCP under conditions where mitochondrial Na/Ca exchange is inhibited. During the recovery, $I_{Ca} = 0$, so that $[Ca^{2+}]_i$ changes under the influence of a net flux ($J_{Extru}+J_{uni}$) that can be measured directly by calculating $-d[Ca^{2+}]_i/dt$. We plotted ($J_{Extru}+J_{uni}$) vs. $[Ca^{2+}]_i$ during the recovery and fit with the following equation:

$$\frac{d[Ca^{2+}]_i}{dt} = -\left(J_{PMCA} + J_{leak} + J_{uni}\right), \quad \text{(A10)}$$

where J_{PMCA} and J_{leak} are as described in Case 1 and

$$J_{uni} = \frac{V_{\max,uni}[Ca^{2+}]_i}{\left(1+\left[\frac{K_{d,uni}}{[Ca^{2+}]_i}\right]^{n_{uni}}\right)}, \quad \text{(A11)}$$

which was approximated by the following equation:

$$J_{uni} \cong \left[\frac{V_{\max,uni}}{K_{d,uni}{}^{n_{uni}}}\right][Ca^{2+}]_i{}^{n_{uni}+1} = A[Ca^{2+}]_i{}^{n_{uni}+1}, \quad \text{(A12)}$$

where A is a constant, which is valid as long as $[Ca^{2+}]_i << K_{d,uni}$. Based on available information, $K_{d,uni} \sim 10$–20 μM, which is 5–10 times the largest measured $[Ca^{2+}]_i$ elevation shown in this study. This approximation was used because it was not possible to obtain unique parameters for Eq. A11 when $[Ca^{2+}]_i$ is low compared with $K_{d.uni}$. While Eq. A12 provided a good description of the $[Ca^{2+}]_i$ dependence of J_{uni}, the parameter values obtained from different sets of measurements ranged widely (Table I). This could be due to the high sensitivity of the parameters to subtle differences in the shape of J_{uni} and/or a functional dependence of A on n_{uni} (see Eq. A12).

The equations describing Ca^{2+} removal are consistent with the finding that in sympathetic neurons treated with Tg and subjected to blockade of the Na/Ca exchanger, the rate of Ca^{2+} removal at each instant in time during the recovery depends on the $[Ca^{2+}]_i$ level at that time. Thus, under these conditions, the time dependence of $(J_{Extru}+J_{uni})$ during the recovery is derived from the time dependence of $[Ca^{2+}]_i$:

$$J_{Extru}(t) + J_{uni}(t) = J_{Extru}\left([Ca^{2+}]_i(t)\right) + J_{uni}\left([Ca^{2+}]_i(t)\right). \quad \text{(A13)}$$

Mitochondrial Na^+/Ca^{2+} Exchanger: J_{NaCa}

To study mitochondrial Ca^{2+} release via the Na^+/Ca^{2+} exchanger, cells were stimulated under the same conditions as in Case 3 but with pipette solutions containing added Na^+. $\tilde{J}_i$ now includes a fourth component ($\tilde{J}_{NaCa}$):

$$\frac{d[Ca^{2+}]_i}{dt} = -\frac{\tilde{J}_{VSCC} + \tilde{J}_{Extru} + \tilde{J}_{uni} + \tilde{J}_{NaCa}}{v_{Cell}(f_i\kappa_i)}$$

$$\frac{d[Ca^{2+}]_{MT}}{dt} = \frac{\tilde{J}_{uni} + \tilde{J}_{NaCa}}{v_{MT}\kappa_{MT}}. \quad \text{(A14)}$$

The equation for $d[Ca^{2+}]_i/dt$ can be rewritten as follows:

$$\frac{d[Ca^{2+}]_i}{dt} = -\left[\frac{I_{Ca}}{2Fv_{Cell}(f_i\kappa_i)} + \left(J_{Extru} + J_{uni} + J_{NaCa}\right)\right], \quad \text{(A15)}$$

where

$$J_{NaCa} = \frac{\tilde{J}_{NaCa}}{v_{Cell}(f_i\kappa_i)}. \quad \text{(A16)}$$

Analysis of J_{NaCa} and its regulation by Ca^{2+} is more complicated than J_{Extru} or J_{uni} because $\tilde{J}_{NaCa}$ depends on the intramitochondrial Ca^{2+} concentration ($[Ca^{2+}]_{MT}$), which was not directly measured in this study. However, Colegrove et al. (2000b) described an approach to measuring a quantity that can be directly related to $[Ca^{2+}]_{MT}$, as long as $[Ca^{2+}]_{MT}$ is proportional to the total concentration, which is assumed here. This approach makes use of the net mitochondrial Ca^{2+} flux (J_{MT}). With information about the time course of J_{MT}, it is possible to obtain information about the dynamics of intramitochondrial Ca concentration. The starting point is provided by the following equation:

$$[Ca^{2+}]_{MT}(t) = [Ca^{2+}]_{MT}(0) + \Delta[Ca^{2+}]_{MT}(t) = [Ca^{2+}]_{MT}(0) + \int_0^t \frac{\tilde{J}_{MT}(t)}{v_{MT}\kappa_{MT}}dt, \quad \text{(A17)}$$

where $[Ca^{2+}]_{MT}(t)$ is the mitochondrial Ca^{2+} concentration at time t, $[Ca^{2+}]_{MT}(0)$ is the resting level of $[Ca^{2+}]_{MT}$, and $\Delta[Ca^{2+}]_{MT}(t)$ is the difference between $[Ca^{2+}]_{MT}(t)$ and $[Ca^{2+}]_{MT}(0)$. As shown below, integration of J_{MT} provides a measure of intramitochondrial Ca^{2+} levels during the recovery that can be used to characterize the functional dependence of $J_{Na/Ca}$ on $[Ca^{2+}]_{MT}$. If mitochondrial Ca^{2+} buffering is fast and low affinity and can be described by a constant buffering factor κ_{MT}, then $[Ca^{2+}]_{MT}$ can be related to measured quantities as follows:

$$\begin{aligned}
[Ca^{2+}]_{MT}(t) &= [Ca^{2+}]_{MT}(0) + \int_0^t \frac{\tilde{J}_{MT}(t)}{v_{MT}\kappa_{MT}}dt \\
&= [Ca^{2+}]_{MT}(0) - \int_t^\infty \frac{\tilde{J}_{MT}(t)}{v_{MT}\kappa_{MT}}dt \\
&= [Ca^{2+}]_{MT}(0) - \int_t^\infty J_{MT}(t)\frac{v_i\kappa_i([Ca^{2+}]_i)}{v_{MT}\kappa_{MT}}dt \\
&= [Ca^{2+}]_{MT}(0) - \frac{v_i}{v_{MT}\kappa_{MT}}\int_t^\infty J_{MT}(t)\kappa_i([Ca^{2+}]_i)dt \\
&= [Ca^{2+}]_{MT}(0) + \frac{v_i}{v_{MT}\kappa_{MT}}\Delta[Ca^{2+}]_{MT}^{(0)}(t) \quad ,
\end{aligned} \quad \text{(A18)}$$

TABLE I

Representative Parameter Values

Plasma Membrane/Cytoplasm	Mitochondria	ER
$k_{leak} = 3.7 \times 10^{-7}\ s^{-1}$	(A,n_{uni}) range: $(4 \times 10^{-4},1)$–$(2 \times 10^{-10}, 3)$	$P_{basal} = 0.01\ s^{-1}$
$V_{max,Extru} = 30\ nMs^{-1}$	(Units of A give nM/s in A12)	$P_{max,RyR} = 0.05\ s^{-1}$
$EC_{50,Extru} = 350$ nM	$\tilde{V}_{max,NaCa} = 4$–$5\ \mu M\ s^{-1}$	$EC_{50,RyR} = 2.6\ \mu M$
$n_{Extru} = 3.5$	$EC_{50,Na/Ca} = 5\ \mu M$	$n_{RyR} = 1$
$f_i\kappa_{Endog} = 40$–90	$[Ca^{2+}]_{MT,rest} \sim 0$ nM	$\tilde{V}_{max,SERCA} = 2.1\ \mu M\ s^{-1}$
$B_{total,fura} = 50$–$90\ \mu M$	$\kappa_{MT} = 4{,}000$	$EC_{50,SERCA} = 30$ nM
$K_{d,Fura} = 224$ nM	$v_{MT}/v_{Cell} = 0.01$	$n_{SERCA} = 2.5$
$D_{Endog} = 0$–$15\ \mu m^2 s^{-1}$		$\kappa_{ER} = 20$
$D_{Ca} = 300\ \mu m^2 s^{-1}$		$v_{ER}/v_{Cell} = 0.04$
$D_{Fura} = 50\ \mu m^2 s^{-1}$		
$v_{Cell} = 35$ pL		
$[Ca^{2+}]_{i,rest} \sim 50$–$100$ nM		

where $\Delta[Ca^{2+}]_{MT}^{(0)}(t)$ is the negative integral of $J_{MT}\kappa_i$ from t to ∞, and the negative integral from t to ∞ has been substituted for the integral from 0 to t, making use of Eq. A19, which is valid as long as stimulus-evoked changes in $[Ca^{2+}]_{MT}$ are reversible (i.e., if $[Ca^{2+}]_{MT}$ eventually returns to its resting level in the aftermath of a stimulus):

$$0 = \int_0^\infty \frac{\tilde{J}_{MT}(t)}{v_{MT}\kappa_{MT}}dt = \int_0^t \frac{\tilde{J}_{MT}(t)}{v_{MT}\kappa_{MT}}dt + \int_t^\infty \frac{\tilde{J}_{MT}(t)}{v_{MT}\kappa_{MT}}dt\,. \tag{A19}$$

An analogous approach was used to evaluate changes in ER Ca^{2+} levels influencing the driving force for Ca^{2+} release via RyRs (Albrecht et al., 2002). To describe the relationship between $J_{Na/Ca}$ and $[Ca^{2+}]_{MT}$ we used the following equation:

$$J_{NaCa}([Ca^{2+}]_{MT}) = -\frac{\tilde{V}_{max,NaCa}}{\left[1+\frac{EC_{50,NaCa}}{[Ca^{2+}]_{MT}}\right]\kappa_i}\,. \tag{A20}$$

Substituting for $[Ca^{2+}]_{MT}$ from Eq. A18 gives a relationship between the measured quantities J_{NaCa}, κ_i, and $\Delta[Ca^{2+}]_{MT}^{(0)}(t)$:

$$J_{NaCa}([Ca^{2+}]_{MT}(t)) = -\frac{\tilde{V}_{max,NaCa}}{\left[1+\left[\frac{EC_{50,NaCa}}{[Ca^{2+}]_{MT}(0)+\frac{v_i}{v_{MT}\kappa_{MT}}\Delta[Ca^{2+}]_{MT}^{(0)}(t)}\right]\right]\kappa_i}\,. \tag{A21}$$

This equation includes four parameters, $\tilde{V}_{max,NaCa}$, $EC_{50,NaCa}$, $[Ca^{2+}]_{MT}(0)$, and $v_i/(v_{MT}\kappa_{MT})$, but can be converted to an equation with three lumped parameters that is more convenient for comparison with data:

$$J_{NaCa}([Ca^{2+}]_{MT}(t)) = -\frac{\tilde{V}_{max,NaCa}}{\left[1+\left[\frac{\left\{EC_{50,NaCa}\frac{v_{MT}\kappa_{MT}}{v_i}\right\}}{\left\{[Ca^{2+}]_{MT}(0)\frac{v_{MT}\kappa_{MT}}{v_i}\right\}+\Delta[Ca^{2+}]_{MT}^{(0)}(t)}\right]\right]\kappa_i} = -\frac{P_3}{\left[1+\left[\frac{P_4}{P_5+\Delta[Ca^{2+}]_{MT}^{(0)}(t)}\right]\right]\kappa_i}, \tag{A22}$$

where

$$P_3 = \tilde{V}_{max,NaCa}$$

$$P_4 = EC_{50,NaCa}\frac{v_{MT}\kappa_{MT}}{v_i} \tag{A23}$$

$$P_5 = [Ca^{2+}]_{MT}(0)\frac{v_{MT}\kappa_{MT}}{v_i}\,.$$

We plotted J_{NaCa} vs. $\Delta[Ca^{2+}]_{MT}^{(0)}(t)$ and fit the data with Eq. A22 to obtain estimates of P_3–P_5, treating this equation as a function of two independent variables, $\Delta[Ca^{2+}]_{MT}^{(0)}$ and $\kappa_i([Ca^{2+}]_i)$, that depend parametrically on time. Given $(\kappa_{MT}v_{MT})/v_i$ and the parameters P_4 and P_5, estimates of $EC_{50,NaCa}$ and $[Ca^{2+}]_{MT}(0)$ can be obtained by dividing the parameters by $(\kappa_{MT}v_{MT})/v_i$. The latter calculation gave an initial value of $[Ca^{2+}]_{MT}$ for simulations.

ER Ca^{2+} Uptake and Release: J_{SERCA}, J_{RyR}

To include contributions from ER Ca^{2+} transport, we used descriptions of Ca^{2+} uptake via SERCAs (J_{SERCA}) and release ($J_{Release}$) from Albrecht et al. (2002) and inserted these into Eqs. M1–M3.

$$\tilde{J}_{SERCA}([Ca^{2+}]_i(t)) = \frac{\tilde{V}_{\max,SERCA}}{\left[1+\frac{EC_{50,SERCA}}{[Ca^{2+}]_i}\right]^{n_{SERCA}}} \quad \text{(A24)}$$

$$\tilde{J}_{Release}([Ca^{2+}]_i,[Ca^{2+}]_{ER}) = \tilde{P}_{ER}([Ca^{2+}]_i - [Ca^{2+}]_{ER}), \quad \text{(A25)}$$

where

$$\tilde{P}_{ER} = \tilde{P}_{ER,Basal} + \frac{\tilde{P}_{\max,RyR}}{\left[1+\frac{EC_{50,RyR}}{[Ca^{2+}]_i}\right]^{n_{RyR}}}. \quad \text{(A26)}$$

The parameters of J_{SERCA} have the conventional meanings. $\tilde{P}_{ER}$ describes the Ca^{2+} permeability of the ER, which consists of a constant, Ca^{2+}-insensitive component ($\tilde{P}_{ER,Basal}$), and a Ca^{2+}-sensitive component that represents the permeability imparted to the ER by ryanodine receptors (RyRs). The latter component has a maximal value $\tilde{P}_{\max,RyR}$, $[Ca^{2+}]_i$ for half maximal activation $EC_{50,\,RyR}$, and cooperativity factor n^{RyR}.

Diffusion Model

We developed a radial model of Ca^{2+} diffusion in a spherical cell consisting of multiple concentric shells and a central sphere (Sala and Hernández-Cruz, 1990; Nowycky and Pinter, 1993; see also Connor and Nikolakopoulou, 1982). Calcium enters the cell across the plasma membrane and diffuses into the interior shells while also being transported by the organelles within each shell. We adopted the fast-buffer approximation (Keener and Sneyd, 1998), which assumes that buffering occurs instantaneously, which is reasonable given the long time scales and continuous stimuli we are considering (Strier et al., 2003). Using this simplification, diffusion leads to changes in Ca^{2+} concentration in the n^{th} shell ($[Ca^{2+}]_{i,n}$) described by Eq. A27:

$$\frac{\partial[Ca^{2+}]_{i,n}}{\partial t} = \frac{(D_{Ca} + D_{Endog}\kappa_{Endog} + D_{Fura}\kappa_{Fura})}{1+\kappa_{Endog}+\kappa_{Fura}}\nabla^2[Ca^{2+}]_{i,n} - \frac{2D_{Fura}\kappa_{Fura}}{1+\kappa_{Endog}+\kappa_{Fura}}|\nabla[Ca^{2+}]_{i,n}|^2, \quad \text{(A27)}$$

where D_{Ca}, D_{Endog}, and D_{Fura} are the diffusion coefficients of cytoplasmic Ca^{2+}, the endogenous buffer, and fura-2, respectively; Ca^{2+} transport by organelles is described by additional terms that are not shown for simplicity. Within each shell, the concentration of free and total calcium in organelles was assumed to be spatially uniform, and direct intraluminal diffusion between shells was not allowed. The gradient was calculated by taking radially symmetric derivatives. Our measurements of cytoplasmic buffering strength provided estimates of $P_1 = f_i(1 + \kappa_{Endog})$ and $P_2 = f_iB_{total,fura}$, which were used to describe buffering in the uniform model (see Eq. M10). For the diffusion model, descriptions of κ_{Endog} and κ_{Fura} were needed. Instead of estimating f_i, which based on a combined mitochondrial and ER volume fraction of ~0.05 would give $f_i \sim 0.95$, and calculating κ_{Endog} and κ_{Fura}, we used the measured parameters directly (equivalent to setting $f_i = 1$), which may lead to an underestimation of the buffering parameters by ~5%. The similarity between calculations based on the diffusion model (with f_i set to unity) and the uniform model (which uses the measured values P_1 and P_2 and makes no assumptions about f_i) when I_{Ca} is small argues that this approximation does not introduce appreciable error.

We integrated the model numerically in a spherically symmetric coordinate system using a partially implicit approach. In this method, the diffusion rates are calculated using the concentration at the next time step, while the fluxes are calculated using the calcium concentration at the previous time step. To check our model, we first made sure that with $I_{Ca} = 0$, resting $[Ca^{2+}]_i$ was steady in all shells. As another check, we made sure calcium was conserved during diffusion. During all of our simulations we calculated the total calcium concentration in the cell in two ways: first by adding the number of moles of calcium in the cytoplasm and all organelles, and second by calculating the starting concentration and then integrating all of the fluxes entering and leaving the cell. We found that these two calculations were within 1% of each other for the diffusion parameters we used, and that this error could be reduced with smaller time and space steps.

Each shell included two organellar compartments that occupy a constant volume fraction of that shell. Since all fluxes were measured based on the impact of the corresponding transport pathway on $[Ca^{2+}]_i$, to describe the impact of these fluxes on organellar Ca^{2+} levels, we multiplied the equations describing organelle transport by $v_{Cell}f_i\kappa_i/v_{MT}\kappa_{MT}$ (for mitochondria) and $v_{Cell}f_i\kappa_i/v_{ER}\kappa_{ER}$ (for ER). $f_i\kappa_i$ was obtained from cytoplasmic Ca^{2+} buffering measurements, and the lumped parameters $v_{Cell}/v_{MT}\kappa_{MT}$ and $v_{Cell}/v_{ER}\kappa_{ER}$ were calculated based on estimates of volume fraction (v_{MT}/v_{Cell}, v_{ER}/v_{Cell}) and buffering strength (κ_{MT}, κ_{ER}).

Simulated Fluorescence-based $[Ca^{2+}]_i$ Measurements

We based fluorescence simulations on those of McHugh and Kenyon (2004). In brief, we calculated

the fluorescence arising from the *n*th shell at two excitation wavelengths:

$$F_{350,n} = S_{f,350}([Fura]_n) + S_{b,350}[CaFura]_n), \quad \text{(A28)}$$

$$F_{380,n} = S_{f,380}([Fura]_n) + S_{b,380}[CaFura]_n), \quad \text{(A29)}$$

where [Fura] and [CaFura] are the concentrations of free and bound fura-2, and $S_{f,350} = 4.97$, $S_{f,380} = 11.3$, $S_{b,350} = 11$, $S_{b,380} = 1$ are parameters describing contributions to fluorescence intensity from free and bound forms of fura-2 satisfying the experimentally determined relations $R_{max} = (S_{b,350}/S_{b,380}) = 11$, $R_{min} = (S_{f,350}/S_{f,380}) = 0.44$, and $(S_{f,380}/S_{b,380}) = 11.3$. The concentration of bound fura-2 in the *n*th compartment ($[CaFura]_n$) is:

$$[CaFura]_n = \frac{[Ca^{2+}]_{i,n} B_{total,fura}}{K_{d,Fura} + [Ca^{2+}]_{i,n}}, \quad \text{(A30)}$$

where $K_{d,Fura} = 224$ nM and $B_{total,fura}$ is the total concentration of fura-2. We calculated the concentration of unbound fura-2 by subtracting $[CaFura]_n$ from $B_{total,fura}$, which is assumed to be constant in all shells. From $F_{350,n}$ and $F_{380,n}$ we calculated the fluorescence ratio in each shell $R_n = F_{350,n}/F_{380,n}$, which can be directly converted to $[Ca^{2+}]_{i,n}$ by the equation (Grynkiewicz et. al., 1985):

$$[Ca^{2+}]_{i,n} = K_{D,Fura}\left(\frac{R_n - R_{min}}{R_{max} - R_n}\right)\frac{S_{f,380}}{S_{b,380}}. \quad \text{(A31)}$$

Average $[Ca^{2+}]_i$ ($[Ca^{2+}]_{i,avg}$) was calculated in two ways (McHugh and Kenyon, 2004). For the first approach,

$$[Ca^{2+}]_{i,avg} = \frac{\sum_{n=0}^{N}[Ca^{2+}]_{i,n} vol_n}{vol_{total}}. \quad \text{(A32)}$$

For the second approach, the total fluorescence was calculated at each of the two excitation wavelengths by summing the fluorescence from each shell, and the ratio was calculated:

$$R_{avg} = \frac{\sum_{n=0}^{N}(S_{f,350}([Fura]_n) + S_{b,350}[CaFura]_n) vol_n}{\sum_{n=0}^{N}(S_{f,380}([Fura]_n) + S_{b,380}[CaFura]_n) vol_n}. \quad \text{(A33)}$$

R_{avg} was then inserted into Eq. A31 to give $[Ca^{2+}]_{i,avg}$.

The authors thank Meredith A. Albrecht and Stephen L. Colegrove for their early contributions to this work and S. Brian Andrews for discussions regarding organellar volume fractions.

This work was supported by a grant from the National Institutes of Health/National Institute of Neurological Disorders and Stroke (NS 33514) to D.D. Friel.

Kenneth C. Holmes served as editor.

Submitted: 7 September 2006
Accepted: 8 December 2006

REFERENCES

Akita, T., and K. Kuba. 2000. Functional triads consisting of ryanodine receptors, Ca^{2+} channels, and Ca^{2+}-activated K^+ channels in bullfrog sympathetic neurons. Plastic modulation of action potential. *J. Gen. Physiol.* 116:697–720.

Albrecht, M.A., S.L. Colegrove, and D.D. Friel. 2002. Differential regulation of endoplasmic reticulum (ER) Ca^{2+} uptake and release rates accounts for multiple modes of Ca^{2+}-induced Ca^{2+} release. *J. Gen. Physiol.* 119:211–233.

Bautista, D.M., M. Hoth, and R.S. Lewis. 2002. Enhancement of calcium signaling dynamics and stability by delayed modulation of the plasma-membrane calcium-ATPase in human T cells. *J. Physiol.* 541:877–894.

Berridge, M.J. 1998. Neuronal calcium signaling. *Neuron.* 21:13–26.

Buntinas, L., K.K. Gunter, G.C. Sparagna, and T.E. Gunter. 2001. The rapid mode of calcium uptake into heart mitochondria (RaM): comparison to RaM in liver mitochondria. *Biochim. Biophys. Acta.* 1504:248–261.

Carafoli, E., L. Santella, D. Branca, and M. Brini. 2001. Generation, control, and processing of cellular calcium signals. *Crit. Rev. Biochem. Mol. Biol.* 36:107–260.

Colegrove, S.L., M.A. Albrecht, and D.D. Friel. 2000a. Dissection of mitochondrial Ca^{2+} uptake and release fluxes in situ following depolarization-evoked $[Ca^{2+}]_i$ elevations in sympathetic neurons. *J. Gen. Physiol.* 115:351–369.

Colegrove, S.L., M.A. Albrecht, and D.D. Friel. 2000b. Quantitative analysis of mitochondrial Ca^{2+} uptake and release pathways in sympathetic neurons: reconstruction of the recovery following depolarization-evoked $[Ca^{2+}]_i$ elevations. *J. Gen. Physiol.* 115:371–388.

Connor, J.A., and G. Nikolakopoulou. 1982. Calcium diffusion and buffering in nerve cytoplasm. *In* Lectures on Mathematics in the Life Sciences. Volume 15. American Mathematical Society, Providence, RI. 79–101.

Cox, D.A., and M.A. Matlib. 1993. A role for the mitochondrial Na^+-Ca^{2+} exchanger in the regulation of oxidative phosphorylation in isolated heart mitochondria. *J. Biol. Chem.* 268:938–947.

Cseresnyes, Z., and M.F. Schneider. 2004. Peripheral hot spots for local Ca^{2+} release after single action potentials in sympathetic ganglion neurons. *Biophys. J.* 86:163–181.

David, G., J. Talbot, and E.F. Barrett. 2003. Quantitative estimate of mitochondrial $[Ca^{2+}]$ in stimulated motor nerve terminals. *Cell Calcium.* 33:197–206.

Dupont, G., and A. Goldbeter. 1993. One-pool model for Ca^{2+} oscillations involving Ca^{2+} and inositol 1,4,5-trisphosphate as coagonists for Ca^{2+} release. *Cell Calcium.* 14:311–322.

Friel, D.D., and R.W. Tsien. 1992. A caffeine- and ryanodine-sensitive Ca^{2+} store in bullfrog sympathetic neurones modulates effects of Ca^{2+} entry on $[Ca^{2+}]_i$. *J. Physiol.* 450:217–246.

Friel, D.D., and R.W. Tsien. 1994. An FCCP-sensitive Ca^{2+} store in bullfrog sympathetic neurons and its participation in stimulus-evoked changes in $[Ca^{2+}]_i$. *J. Neurosci.* 14:4007–4024.

Friel, D.D. (2003) Mitochondrial and ER-calcium uptake and release fluxes and their interplay in intact nerve cells. *In* Understanding Calcium Dynamics, Lecture Notes in Physics.Volume 623. M. Falcke and H. Malchow, editors. Springer-Verlag, Berlin. 37–65.

Goldbeter, A., G. Dupont, and M.J. Berridge. 1990. Minimal model for signal-induced Ca^{2+} oscillations and for their frequency encoding through protein phosphorylation. *Proc. Natl. Acad. Sci. USA.* 87(4):1461–1465.

Grynkiewicz, G., M. Poenie, and R.Y. Tsien. 1985. A new generation of Ca^{2+} indicators with greatly improved fluorescence properties. *J. Biol. Chem.* 260:3440–3450.

Gunter, K.K., and T.E. Gunter. 1994. Transport of calcium by mitochondria. *J. Bioenerg. Biomembr.* 26:471–485.

Herrington, J., Y.B. Park, D.F. Babcock, and B. Hille. 1996. Dominant role of mitochondria in clearance of large Ca^{2+} loads from rat adrenal chromaffin cells. *Neuron.* 16:219–228.

Hongpaisan, J., N.B. Pivovarova, S.L. Colegrove, R.D. Leapman, D.D. Friel, and S.B. Andrews. 2001. Multiple modes of calcium-induced calcium release in sympathetic neurons II: A $[Ca^{2+}]_i$-dependent transition from Ca^{2+} accumulation to net release from the endoplasmic reticulum and its spatiotemporal characteristics. *J. Gen. Physiol.* 118:101–112.

Hua, S.Y., M. Nohmi, and K. Kuba. 1993. Characteristics of Ca^{2+} release induced by Ca^{2+} influx in cultured bullfrog sympathetic neurones. *J. Physiol.* 464:245–272.

Jones, S.W., and T.N. Mark. 1989. Calcium currents in bullfrog sympathetic neurons. I. Activation kinetics and pharmacology. *J. Gen. Physiol.* 94:151–167.

Kao, J.P., and R.Y. Tsien. 1988. Ca^{2+} binding kinetics of fura-2 and azo-1 from temperature-jump relaxation measurements. *Biophys. J.* 53:635–639.

Keener, J.P., and J. Sneyd. 1998. Mathematical Physiology. Springer-Verlag, New York. 341–343.

Kovacs, L., E. Rios, and M.F. Schneider. 1983. Measurement and modification of free calcium transients in frog skeletal muscle fibres by a metallochromic indicator dye. *J. Physiol.* 343:161–196.

Liang, H., C.D. DeMaria, M.G. Erickson, M.X. Mori, B.A. Alseikhan, and D.T. Yue. 2003. Unified mechanisms of Ca^{2+} regulation across the Ca^{2+} channel family. *Neuron.* 39:951–960.

McDonough, S.I., Z. Cseresnyes, and M.F. Schneider. 2000. Origin sites of calcium release and calcium oscillations in frog sympathetic neurons. *J. Neurosci.* 20:9059–9070.

McHugh, J.M., and J.L. Kenyon. 2004. An Excel-based model of Ca^{2+} diffusion and fura 2 measurements in a spherical cell. *Am. J. Physiol. Cell Physiol.* 286:C342–C348.

Means, S., A.J. Smith, J. Shepherd, J. Shadid, J. Fowler, R.J. Wojcikiewicz, T. Mazel, G.D. Smith, and B.S. Wilson. 2006. Reaction diffusion modeling of calcium dynamics with realistic ER geometry. *Biophys. J.* 91:537–557.

Mogami, H., J. Gardner, O.V. Gerasimenko, P. Camello, O.H. Petersen, and A.V. Tepikin. 1999. Calcium binding capacity of the cytosol and endoplasmic reticulum of mouse pancreatic acinar cells. *J. Physiol.* 518:463–467.

Neher, E., and G.J. Augustine. 1992. Calcium gradients and buffers in bovine chromaffin cells. *J. Physiol.* 450:273–301.

Nicholls, D.G., and S. Chalmers. 2004. The integration of mitochondrial calcium transport and storage. *J. Bioenerg. Biomembr.* 36:277–281.

Nowycky, M.C., and M.J. Pinter. 1993. Time courses of calcium and calcium-bound buffers following calcium influx in a model cell. *Biophys. J.* 64:77–91.

Pivovarova, N.B., J. Hongpaisan, S.B. Andrews, and D.D. Friel. 1999. Depolarization-induced mitochondrial Ca accumulation in sympathetic neurons: spatial and temporal characteristics. *J. Neurosci.* 19:6372–6384.

Pozzo-Miller, L.D., N.B. Pivovarova, R.D. Leapman, R.A. Buchanan, T.S. Reese, and S.B. Andrews. 1997. Activity-dependent calcium sequestration in dendrites of hippocampal neurons in brain slices. *J. Neurosci.* 17:8729–8738.

Robb-Gaspers, L.D., P. Burnett, G.A. Rutter, R.M. Denton, R. Rizzuto, and A.P. Thomas. 1998. Integrating cytosolic calcium signals into mitochondrial metabolic responses. *EMBO J.* 17:4987–5000.

Sala, F., and A. Hernández-Cruz. 1990. Calcium diffusion modeling in a spherical neuron. Relevance of buffering properties. *Biophys. J.* 57:313–324.

Schuhmeier, R.P., and W. Melzer. 2004. Voltage-dependent Ca^{2+} fluxes in skeletal myotubes determined using a removal model analysis. *J. Gen. Physiol.* 123:33–51.

Sipido, K.R., and W.G. Wier. 1991. Flux of Ca^{2+} across the sarcoplasmic reticulum of guinea-pig cardiac cells during excitation-contraction coupling. *J. Physiol.* 435:605–630.

Strier, D.E., A.C. Ventura, and S.P. Dawson. 2003. Saltatory and continuous calcium waves and the rapid buffering approximation. *Biophys. J.* 85:3575–3586.

Suzuki, S., M. Osanai, N. Mitsumoto, T. Akita, K. Narita, H. Kijima, and K. Kuba. 2002. Ca^{2+}-dependent Ca^{2+} clearance via mitochondrial uptake and plasmalemmal extrusion in frog motor nerve terminals. *J. Neurophysiol.* 87:1816–1823.

Thayer, S.A., and R.J. Miller. 1990. Regulation of the intracellular free calcium concentration in single rat dorsal root ganglion neurones in vitro. *J. Physiol.* 425:85–115.

Wanaverbecq, N., S.J. Marsh, M. Al-Qatari, and D.A. Brown. 2003. The plasma membrane calcium-ATPase as a major mechanism for intracellular calcium regulation in neurones from the rat superior cervical ganglion. *J. Physiol.* 550:83–101.

Weber, C.R., K.S. Ginsburg, K.D. Philipson, T.R. Shannon, and D.M. Bers. 2001. Allosteric regulation of Na/Ca exchange current by cytosolic Ca in intact cardiac myocytes. *J. Gen. Physiol.* 117:119–131.

Weibel, E.R., and H. Elias. 1967. Introduction to stereologic principles. *In* Quantitative Methods in Morphology. E.R. Weibel and H. Elias, editors. Springer-Verlag, Berlin. 89–98.

Wennemuth, G., D.F. Babcock, and B. Hille. 2003. Calcium clearance mechanisms of mouse sperm. *J. Gen. Physiol.* 122:115–128.